CHALMERS

Thermo-Mechanical-Metallurgical Modelling of Pearlitic Steels and Railhead Repair Welding

BJÖRN ANDERSSON

Department of Industrial and Materials Science
CHALMERS UNIVERSITY OF TECHNOLOGY
Göteborg, Sweden 2024

THESIS FOR THE DEGREE OF DOCTOR OF PHILOSOPHY IN SOLID AND STRUCTURAL MECHANICS

Thermo-Mechanical-Metallurgical Modelling of Pearlitic Steels and Railhead Repair Welding

BJÖRN ANDERSSON

Department of Industrial and Materials Science
Division of Material and Computational Mechanics
CHALMERS UNIVERSITY OF TECHNOLOGY

Göteborg, Sweden 2024

Thermo-Mechanical-Metallurgical Modelling of
Pearlitic Steels and Railhead Repair Welding
BJÖRN ANDERSSON
ISBN 978-91-8103-017-4

Doktorsavhandlingar vid Chalmers tekniska högskola
Ny serie nr. 5475
ISSN 0346-718X
Department of Industrial and Materials Science
Division of Material and Computational Mechanics
Chalmers University of Technology
SE-412 96 Göteborg
Sweden
Telephone: +46 (0)31-772 1000

Chalmers Reproservice
Göteborg, Sweden 2024

Thermo-Mechanical-Metallurgical Modelling of
Pearlitic Steels and Railhead Repair Welding
BJÖRN ANDERSSON
Department of Industrial and Materials Science
Division of Material and Computational Mechanics
Chalmers University of Technology

Abstract

The efficiency of rail transport is attributed to low rolling resistance, which comes at the cost of high contact pressures between rail and wheel. Consequently, both the rail and wheel can be susceptible to fatigue crack initiation and propagation due to the resulting high stresses and large number of load cycles in service. Therefore, the mechanical performance of the rail and wheel material is critical for safe operation. Thermal loading, such as that caused by wheel locking or railhead repair welding, can cause gradual or drastic changes in local material behaviour, resulting in significant detrimental effects to the rail and wheel. This thesis presents a phenomenological modelling framework for numerical simulations of the thermo-metallurgical-mechanical behaviour of pearlitic railway steels during and after high-temperature thermal loading.

The framework consists of a material model that incorporates cyclic hardening plasticity, phase transformation kinetics, transformation-induced plasticity, multi-phase homogenisation, and recovery of the virgin material state after cyclic melting and solidification. The ability of the model to simulate intricate thermo-metallurgical-mechanical behaviour is demonstrated in quasi-static material point simulations. The material model is implemented in a finite element framework to obtain a simulation-based tool that balances computational efficiency, simulation fidelity, and engineering applicability. Several simulations demonstrate the effectiveness of this tool, including simulations of a wheel flat, laser-induced martensitic patches on the rail surface, and railhead repair welding processes. The simulation-tool is also validated against experimental data, in terms of residual material states after high-temperature processes.

The thesis provides insights into the evolution of material phases and stresses under thermal loading in high-temperature railway processes, as well as the redistribution of residual stresses during subsequent operational loading conditions. For instance, simulations of the railhead repair welding process indicate that pre-heating has a minor impact on the quality of the repair, while the welding build-up paths have a significant impact. The simulations also highlight the critical region for fatigue crack initiation by showing how residual tensile stresses are reduced near the surface of the rail or wheel and increased at some distance below during operation for the repaired rail.

Keywords: Pearlitic steels, Phase transformations, Homogenisation, Cyclic plasticity, Finite element analysis, Railhead repair, Welding simulations

Preface

The research presented in this thesis was carried out during the period of April 2019 to March 2024 at the department of Industrial and Materials Science at Chalmers University of Technology within the research project MU37 "Numerical simulations of welding and other high-temperature processes". The research is part of the on-going activities within CHARMEC – Chalmers Railway Mechanics (`www.chalmers.se/charmec`). Parts of the project have been funded from the European Union's Horizon 2020 research and innovation programme in the project In2Track2 and In2Track3 under grant agreement Nos 826255 and 101012456. Funding has also been received from the Horizon Europe research and innovation programme under IAM4RAIL with grant agreement number 101101966.

All numerical computations performed in the research work were enabled by resources provided by Chalmers e-Commons at Chalmers (C3SE) and by the National Academic Infrastructure for Supercomputing in Sweden (NAISS) and the Swedish National Infrastructure for Computing (SNIC) at C3SE partially funded by the Swedish Research Council through grant agreements no. 2022-06725 and no. 2018-05973.

Acknowledgements

I would like to start by expressing my sincere gratitude to my supervisors, Professor Magnus Ekh, Professor Johan Ahlström, and Professor Lennart Josefson. You are all incredible. The support, guidance and encouragement you have given me throughout this journey has been more than I could have ever hoped for. I have truly enjoyed working with you.

I would also like to thank all research partners and my co-authors. Your valuable insights and contributions have greatly improved the quality of the thesis.

Furthermore, I want to express my appreciation for all my colleagues at the Division of Material and Computational Mechanics and the Division of Dynamics. Our pleasant work environment, engaging discussions, and daily laughter always brightened my day.

I would also like to thank my friends and family for the patience and understanding you have shown me throughout this challenging yet rewarding journey. Last but certainly not least, I want to thank to my girlfriend Katarina. Your love means the world to me.

Göteborg, March 2024
Björn Andersson

Thesis

This thesis consists of an extended summary and the following appended papers:

Paper A Ali Esmaeili, Johan Ahlström, Björn Andersson, Magnus Ekh, Modelling of cyclic plasticity and phase transformations during repeated local heating events in rail and wheel steels, *International Journal of Fatigue*, 151, (2021), 106361, DOI: 10.1016/j.ijfatigue.2021.106361

Paper B Björn Andersson, Johan Ahlström, Magnus Ekh, B Lennart Josefson, Homogenization based macroscopic model of phase transformations and cyclic plasticity in pearlitic steel, *Journal of Thermal Stresses*, 45:6, 470-492, (2022) DOI:10.1080/01495739.2022.2056557

Paper C Björn Andersson, Magnus Ekh, B Lennart Josefson, Computationally efficient simulation methodology for railway repair welding: Cyclic plasticity, phase transformations and multi-phase homogenization, *Journal of Thermal Stresses*, 47:2, 164-188, (2023), DOI: 10.1080/01495739.2023.2283309

Paper D Erika Steyn, Björn Andersson, Johan Ahlström, Thermal Pulses on Pearlitic Steels: Influence of laser scanning parameters on surface layers transforming to martensite, *Manuscript submitted for publication*

Paper E Björn Andersson, Erika Steyn, Magnus Ekh, B Lennart Josefson, Simulation-Based Assessment of Railhead Repair Welding Process Parameters, *Manuscript submitted for publication*

The attached Papers were prepared in collaboration with the co-authors. In Paper A, the author of this thesis contributed to the implementation and simulations of the models, participated in the post-processing of the results, and was involved in both the writing and the peer-review process. In papers B, C and E, the author of this paper was responsible for the majority of the work, including planning and writing the papers, developing the theory, implementing the numerical models, running the simulations, and managing the submission and peer review process. For paper D, the author of this paper participated in the planning and writing of the paper, and was responsible for the development of the theory, implementation of the numerical models, and execution of the simulations.

Contents

Part I
Extended Summary

1 Introduction

1.1 Background and motivation

The historical impact of railway networks on shaping our industrial society is undeniable. One simple but powerful illustration of this leading influence is the introduction of the standard time system. Other examples include significant contributions to economic development and social progress in regions where extensive railway infrastructure was first established and expanded, such as Western Europe, Japan and North America. These contributions were realised through improvements in the efficiency of inland transport and long-distance public mobility, factors which in many respects still constitute the primary advantages of railways over road transport [1].

These historical factors that made the railway industry an engine of progress also extend into our future, firmly establishing railways as an integral part of sustainable development. Acknowledging the often superficial use of the term sustainable, railways do in fact contribute both directly and indirectly to the realisation of several of the United Nations' 17 Sustainable Development Goals (SDGs) [2]. Concrete examples are found in SDG 9: Industry, Innovation, and Infrastructure; SDG 11: Sustainable Cities and Communities; SDG 12: Responsible Consumption and Production; and SDG 13: Climate Action, where the major contribution for all goals lies in the role of railways as an energy-efficient and low-emission mode of transportation.

Empirical studies consistently confirm that rail transport has a low environmental impact, producing the lowest CO_2 emissions per distance travelled and per tonne transported [3]. This is particularly true for inland freight transport, where emissions per tonne transported are around a tenth of those of road freight. Similarly, other authoritative reports urge a shift towards rail and water transport to meet global mandates to cut emissions [4, 5]. Recent statistics indicate an upward trend in European passenger train occupancy rates and rail freight loads over the past decade, providing minor consolation in the otherwise grim state of SDG realisation [6]. Nevertheless, the effective use of available technologies, resources and collective knowledge is crucial for shaping a better future. In light of this, growing demands on rail networks require increased reliability and efficiency, which especially relates to the context of the work presented in this thesis.

The contact interface between the rail and the train wheels is crucial to the high efficiency of rail transport. The use of hard materials in both components, i.e. (relatively) high carbon steel, minimises rolling resistance but also results in exceptionally high contact

pressures [7, 8, 9]. As the wheel traverses the rail surface, the resulting rolling contact load generates a complex multiaxial stress state comprising high compressive and shear stresses. These stresses place severe demands on the materials of both rail and wheel and, combined with the immense number of wheel passes over a given material point, can lead to fatigue damage. In addition, trends in the ongoing efforts to improve the competitiveness of rail transport point towards increased traffic, higher speeds and higher axle loads [10, 11, 12]. Each of these factors alone increases the stress on the track system, presenting inevitable challenges in terms of increased fatigue damage and wear, as well as increasing the need for effective rail maintenance.

The primary objectives of rail maintenance are to restore the railhead profile and to remove discrete railhead defects. Typically, the former is achieved by grinding or milling, while the latter involves welding to either replace entire rail sections or perform in-situ railhead repairs. These operations expose the rail to significant thermal loads, potentially inducing undesirable microstructures and detrimental residual stress states. Intense localised thermal loading may also occur under operational loading conditions, such as poor wheel-rail friction. Combined with the high magnitude contact stresses and large number of rolling contact load cycles, this can have devastating consequences. Therefore, a comprehensive understanding of the high-temperature thermo-metallurgical-mechanical behaviour of railway steels is essential for designing and planning rail maintenance processes, as well as defining safe operating conditions.

At the Centre of Excellence in Railway Mechanics at Chalmers (CHARMEC), the thermo-metallurgical-mechanical behaviour of railway steels has been studied both experimentally, e.g. [13, 14, 15, 16], and with numerical simulation tools, e.g. [17, 18, 19, 20, 21]. These studies confirm that localised high temperature events can adversely affect the structural integrity of railway components. Furthermore, the research highlights the critical role of accurate simulation models in assessing the consequences under operational conditions. To improve simulation fidelity, it is important to advance modelling by focusing on the coupling between phase transformations and temperature-dependent cyclic mechanical behaviour. Advances in simulation-based tools are equally important to facilitate large-scale simulations of high-temperature processes, in particular to analyse how the material state after high-temperature processes is affected by subsequent operational loading conditions. This background is the main motivation for the work presented in this thesis. This is where we start.

1.2 Research objectives

The work presented in this thesis is part of the CHARMEC project *MU37 - Welding and other high temperature operations in steel*. The main objective of the project was to improve numerical simulation tools for modelling high temperature operations on railway steels. The main research objectives of this thesis are as follows:

- Develop sufficiently advanced numerical tools to gain insights into the thermo-metallurgical-mechanical material behaviour during cyclic high-temperature (close to and above the melting temperature) processes. Assess and improve existing material models for accurate predictions of residual stresses and material phase evolution in railway applications.
- Implement the developed material model within a finite element framework, carefully balancing computational limitations, simulation fidelity, and engineering objectives. Explore and advance the capabilities of numerical tools to simulate full-scale high-temperature processes in railway components.
- Using the developed numerical tools, enhance the understanding of how operational loading conditions may impact the material state resulting from high-temperature events in railway steels. Ensure simulation precision through validation against experimental and field data.
- Present a simulation-based assessment tool which can be used to investigate consequences and mechanical performance following high-temperature processes in railway operations. This tool should provide accurate and predictive methods to support technology development and design of maintenance procedures in the railway industry.

1.3 Scope and limitations

When working towards research objectives, it is crucial to recognise inherent limitations and also to impose limits on the scope of the work. For instance, computational constraints will restrict the proposed material models to be of macroscopic type. A multiscale type of material modelling would therefore not be computationally feasible for the targeted railway applications in this project. The accuracy of the models and simulations will rely on the availability and quality of experimental data for calibration and validation, both in terms of material and process data. Additionally, the complexity of real-world conditions, combined with the challenges of multi-scale and multi-physics simulations, will introduce unavoidable inaccuracies in the simulation results. The scope of this study is limited to pearlitic rail and wheel steels, and extending the findings to other steel compositions may require further investigation. Furthermore, the study is restricted to two high-temperature processes for railway components: hard train wheel braking and railhead repair welding. The evaluation of the simulation results will focus mainly on on stresses, phase transformations, and fatigue crack initiation.

2 Railway steels

2.1 Rail and wheel materials

The production of all metal objects involves heating and cooling processes at various stages of manufacturing. For steel alloys, these processes include both liquid-to-solid and solid-to-solid phase transformations. In its solid state, the base metal for steel, iron, exists in different crystalline structures (allotropic forms) depending on the temperature and its rate of change. These crystalline structures, combined with alloying elements, provide a wide range of possible properties. Interstitial carbon solutes are of particular importance as they hinder dislocation movement during deformation and influence transformations due to the varying solubility of carbon in different crystalline structures. For example, the face-centred cubic (FCC) structure of the austenite phase, which is stable at elevated temperatures, allows for more interstitial carbon than the body-centred cubic (BCC) structure of the ferrite phase, which is stable at lower temperatures [22, 23].

The appended papers focus on local heating events in railway steels and the resulting mechanical and metallurgical changes. Two common railway steels are examined: ER7T wheel steel (**Papers A** and **D**) and R260 rail steel (**Papers B**, **C**, **D** and **E**), with their respective chemical compositions shown in Table 2.1. At these near eutectoid compositions (close to 0.77 wt% carbon), austenite primarily transforms into pearlite, i.e. a two-phase microstructure consisting of lamellar arrangements of ferrite and cementite, with nearly all of the carbon bound in the cementite phase. The lamellar network makes pearlite ductile and relatively wear resistant, making it well suited to both railway wheels and rails. Examples of the wheel and rail microstructures, obtained from [24], are shown in Figure 2.1.

Table 2.1: Typical chemical compositions of train wheel steel grade ER7T and rail steel grade R260 [25, 26].

[wt %]	C	Mn	Si	Cr	Ni	Cu	Mo	P	S	V	Fe
ER7T	0.52	0.8	0.4	0.3	0.3	0.3	0.08	0.02	0.02	0.06	bal.
R260	0.74	1.25	0.6	0.15	0.1	0.15	0.02	0.03	0.03	0.03	bal.

Figure 2.1 demonstrates that both materials exhibit an almost fully pearlitic microstructure after manufacturing, despite the hypoeutectoid compositions. The wheel material obtains a finer lamellar spacing due to intricate cooling procedures, and has some free ferrite. The rail, with its higher carbon content, has no free ferrite and a higher cementite volume fraction. This comparison of microstructure supports an important aspect mentioned in **Paper B** and discussed in detail in **Paper D**. Namely, both materials have similar mechanical properties, such as comparable strength and cyclic plastic behaviour at room temperature, but differ in their phase transformation kinetics. This

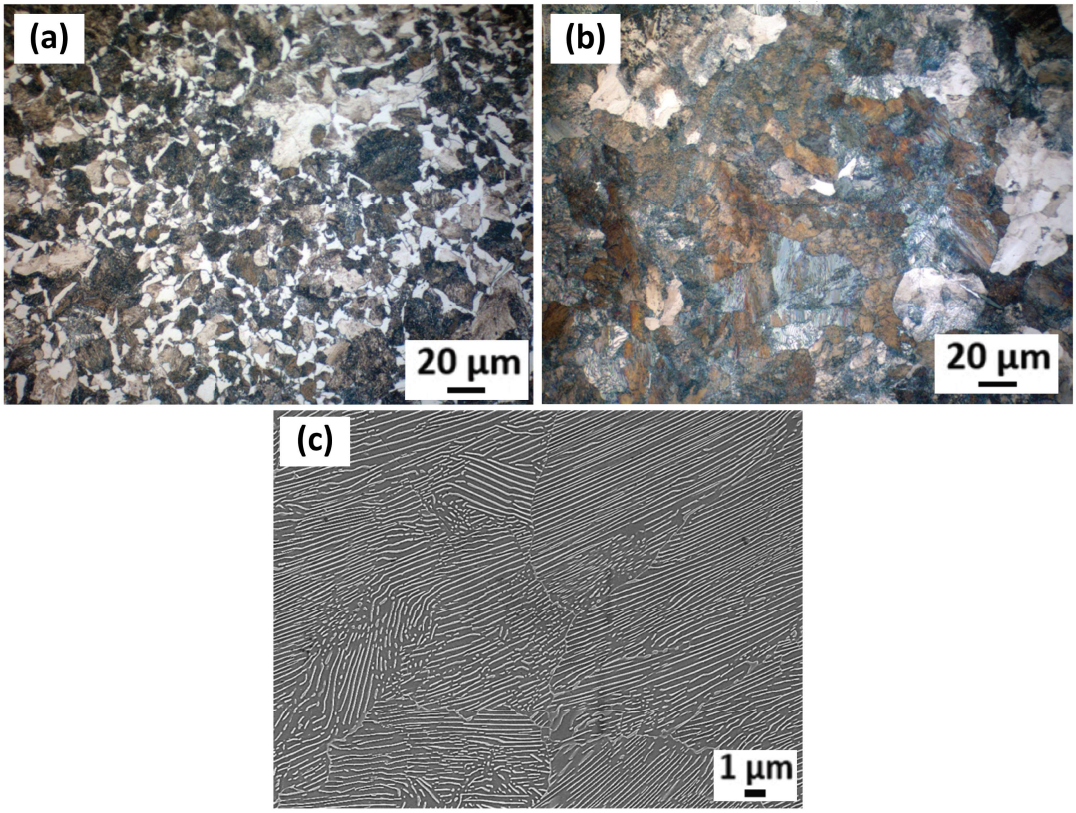

Figure 2.1: *Pearlitic railway steel microstructures, reprinted from [24] with permission. Low magnification light optical micrographs of the ER7T wheel material (a) and (b) R260 rail material. (c) High magnification scanning electron micrographs for R260 rail material.*

observation supports the use of wheel material mechanical data in the absence of rail data, coupled with material-specific transformation data from JMatPro, for the analyses presented in **Papers B**, **C** and **E**. It should also be noted that this assumption is further justified by the comparative nature of the respective analyses.

2.2 Phase transformations

The main focus of this thesis is on macroscopic simulations using a phenomenological modelling approach, whereby several simplifications and discretisations are introduced in the following chapters. Regarding phases and phase transformations, no strict distinction is made between phases or microstructure. Instead, all basic forms of steel are referred to as material phases. Moreover, as only near-eutectioid wheel and rail steels are considered, not all possible phases or transformations are studied in this thesis, for simplicity. Those considered are described briefly in the following text for the processes of heating, cooling and reheating. Extensive descriptions can be found in e.g. [22, 23].

Heating

In all of the attached papers, the initial pearlitic material is subjected to heating above the austenite transformation temperature, resulting in the diffusive transformation of pearlite to austenite. This process is influenced by the morphology of the material, the carbon content and the heating rate. Higher heating rates result in increased austenitisation temperatures, as demonstrated in the time-temperature austenitisation (TTA) diagram in Figure 2.2. At these temperatures, austenite has a hardness similar to its pearlitic parent phase but with increased ductility due to its denser crystalline structure having more slip planes [27, 28, 29]. With continued heating, as considered in **Papers C**, **D** and **E**, the solid-to-liquid transformation takes place and the austenite melts. Therefore, a liquid-like melted material phase was introduced for reasons discussed in Chapter 3. Regarding the austenitisation, it should be noted that for the material composition presented in Table 2.1, the software used to produce the austenitisation data (JMatPro [30]) presented in Figure 2.2b predicts that the alloying elements will give an effective eutectic point below the R260 carbon content of 0.74 wt%. Hence the A_{cm} transformation line representing the cementite transformation.

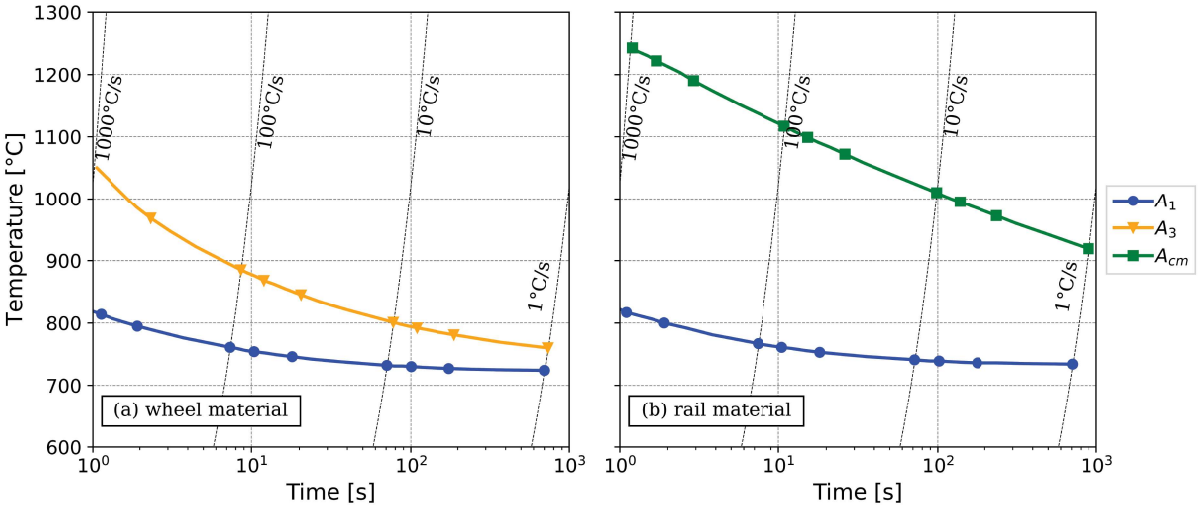

Figure 2.2: *Time Temperature Austenitisation (TTA) diagrams for (a) ER7T wheel material and (b) R260 rail material, based on data obtained from JMatPro [30]. A_1 represents pearlite to austenite transformation, A_3 represents ferrite to austenite transformation and A_{cm} represents cementite to austenite transformation. Dashed diagonal lines represent different heating rates.*

Slow cooling

When cooled, the melted steel (modelled as a liquid-like state) solidifies into austenite. In continued cooling and depending on the cooling rate, the continuous cooling transformation

(CCT) diagram presented in Figure 2.3 shows that several phase transformations are possible. In the case of slow cooling rates, which are relevant to the heat affected zone (HAZ) in the repair welding processes considered in **Papers C** and **E**, a diffusive pearlitic transformation occurs, resulting in slightly different microstructures for hypo-, hyper-, or eutectoid steels. In short, eutectoid steel produces a fully pearlitic microstructure, while hypoeutectoid steel results in pearlite nodules surrounded by ferrite, and hypereutectoid steel results in pearlite grains surrounded by cementite [27, 28, 29]. It is important to note that for the hypoeutectoid wheel steel cases discussed in **Papers A** and **D**, the cooling rates are high, and therefore, the austenite to ferritic-pearlitic transformation is not considered.

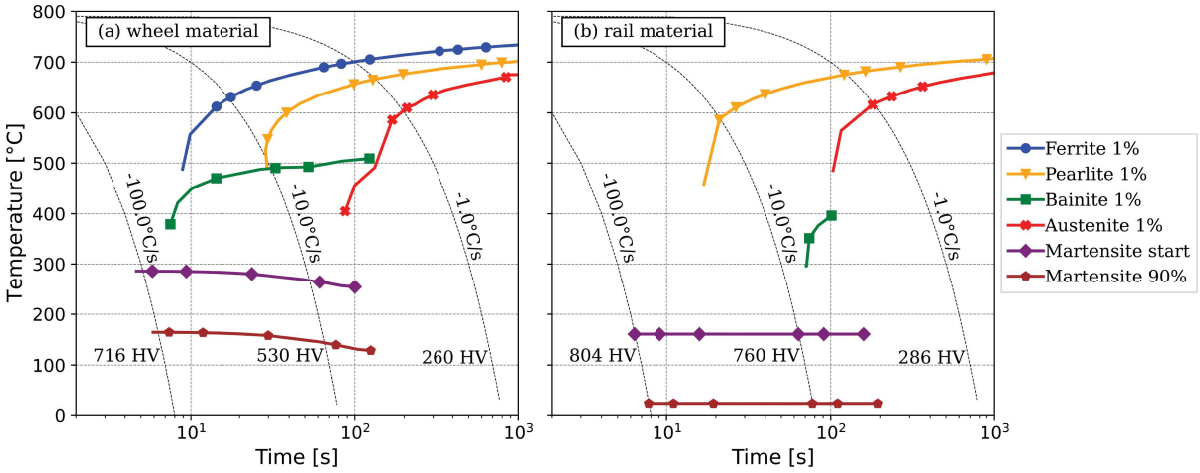

Figure 2.3: *CCT diagrams for (a) ER7T wheel material and (b) R260 rail material, based on data obtained from JMatPro [30]. Dashed diagonal lines represents different cooling rates.*

Rapid cooling

At high cooling rates, i.e. quenching, insufficient time for carbon diffusion leads to unstable austenite followed by very rapid diffusionless transformation to martensite. This transformation is highly relevant in multi-pass welding. The resulting microstructure has a carbon-supersaturated body-centred tetragonal lattice structure which causes substantial shear and volume expansion. Applied stress during this transformation results in transformation induced plasticity (TRIP), which is characterised by a significant local plastic effect and an orientation effect. It is particularly important in processes involving local heating, as volume changes are constrained by the surrounding material. The TRIP effect was therefore introduced in **Paper B** and incorporated into subsequent works. The martensite transformation is considered to be an athermal process governed by the degree of undercooling below its transformation start temperature. As discussed in detail in **Paper D**, most alloying elements contribute to the lowering of the starting temperature,

with interstitial carbon and nitrogen having the most significant influence. The carbon content also affects the strength and hardness of martensite through interstitial hardening and through the sheared lattice structure which produces high densities of dislocations and twinning [27, 28, 29]. This brittleness makes martensite potentially detrimental in railway applications and investigating its consequences is a key aspect of the appended papers.

Moderate cooling

In the intermediate temperature range between the high-temperature pearlite transformation and the low-temperature martensite transformation, the bainite transformation takes place, as shown in Figure 2.3. This results in a microstructure with finely dispersed plate- or lath-like cementite and ferrite. As carbon diffusion is somewhat restricted at these temperatures, the nature of the bainitic transformation is both displacive and diffusional. Similar to martensite, bainite grows without diffusion, but due to the elevated temperatures, carbon from the ferrite partitions back into the residual austenite or precipitates as cementite, distinguishing upper and lower bainite [27, 28, 29]. However, this work does not distinguish between these forms. Furthermore, as observed for the weld filler metals in **Papers C** and **E**, bainite transformation is facilitated by alloying elements that retard ferrite and pearlite transformations.

Reheating

When carbon-supersaturated metastable phases are subjected to a second heating below austenitisation in a process known as tempering, excess carbon precipitates as carbides, while substitutional solutes remain unaffected. Tempering of martensite results in coarse carbides in a ferritic matrix, increasing its ductility while maintaining high strength. Tempering mechanisms occur in steps with overlapping temperature ranges. Steels with high martensite starting temperatures experience some degree of auto-tempering during transformation. Tempering is primarily driven by non-equilibrium phases obtaining a more stable state, whereby bainite also experiences tempering. Due to its high transformation temperatures, autotempering is unavoidable. This makes bainite less sensitive to additional tempering reheat treatments [27, 28, 29]. For the railway related processes considered in this thesis, tempering is not the result of an additional heat treatment to improve mechanical properties. Instead, it is an accidental reheating in **Paper A** and an inherent reheating processes in **Papers C**, **D** and **E**.

3 Material modelling

3.1 Phase transformation kinetics

As explained in the previous chapter, the thermo-metallurgical-mechanical behaviour of steel is complex and the material properties change significantly during heating and cooling, where solid-state phase transformations result in permanent changes. The literature on modelling these transformations and the resulting mechanical behaviour spans half a century, with different approaches depending on the intended application. Anisothermal phenomenological models commonly use the well-established Johnson-Mehl-Avrami-Kolmogorov (JMAK) equation for diffusive transformations and the Koistinen and Marburger (KM) equation for displacive transformations, see e.g [31, 32, 33]. Alternative approaches using exponential functions or differential equations to capture the typical behaviour of gradual to rapid to gradual nucleation rate for diffusive transformations have also proved useful, see e.g. [34, 35]. For simulations involving both heating and cooling cycles, linear approximations to the initial austenite transformation can be used to simplify the modelling, see e.g. [36]. Furthermore, although not considered in the appended papers, several works in the literature modelling the isothermal transformations using a thermodynamic transformation potential or driven by the stress-strain state of the material, see e.g. [37, 38, 39]. At an even greater level of detail, other works present phase transformation modelling using various multi-scale and phase field approaches, see e.g. [40, 41].

In the attached papers, the modelling of phase transformation kinetics use an anisothermal phenomenological modelling approach using the aforementioned JMAK and KM equations. **Paper A** introduces the implementation of the modelling framework, which is then expanded in **Papers B** and **C**. The material phases considered are identified by the following indices: austenite (a), pearlite (p), bainite (b), martensite (m), tempered martensite (tm), and a liquid-like phase (ℓ). The phase volume fractions, p_{x}, indicate the amount of each phase present at each time instance, with the constraint that their sum must always equal 1:

$$\sum_x p_x = 1 \quad \text{for } x = \mathrm{a}, \quad \mathrm{p}, \quad \mathrm{b}, \quad \mathrm{m}, \quad \mathrm{tm}, \quad \ell \tag{3.1}$$

The underlying physics of the phase transformations is briefly presented in Section 2.2. Using a similar structure, this section presents a summary of the corresponding modelling during heating, cooling and reheating. It is important to note that the same volume fraction variable, $p_{\mathrm{x}}(t;T)$, is calculated using different formulas depending on the temperature range and the rate of heating or cooling.

Heating

As stated in Section 2.2, the transformation kinetics for heating above the austenitisation temperature are described by TTA-diagrams (similar to Figure 2.2). In the numerical implementations, presented in **Paper A**, line A_1 represents the temperature at which 1% of the pearlite has transformed into austenite, while A_3 and A_{cm} represent the temperature at which 99% of the pearlite has transformed. The transformation kinetics of the decreasing pearlite volume fraction, p_p, for a constant temperature, T, is described by the JMAK equation, cf. [42, 43]:

$$p_\mathrm{p}(t;T) = p_\mathrm{p}(\check{t}) \exp\left(-b_\mathrm{p}(T)\,(t-\check{t})^{n_\mathrm{p}(T)}\right) \tag{3.2}$$

where $n_\mathrm{p}(T)$ is the Avrami exponent, $b_\mathrm{p}(T)$ is the overall nucleation rate constant at holding temperature T, and $\check{t}$ is the "virtual time" required for transforming the initial volume fraction $p_\mathrm{p}(\check{t})$ of pearlite into austenite. This somewhat awkward formulation is used to handle varying temperatures using the Scheil's additive rule [44] following the implementation presented by [45]. Equation 3.2 thereby describes how the pearlite volume fraction, $p_\mathrm{p}(t;T)$, decreases exponentially with holding time t at temperature T from its initial fraction $p_\mathrm{p}(\check{t})$. When multiple phases are present, the total amount of nucleated austenite can be calculated by summing the decrease in volume fractions of the parent phases during austenitisation:

$$p_\mathrm{a}(t;T) = p_\mathrm{a}(\check{t}) + \sum_x \left(p_x(\check{t}) - p_x(t;T)\right) \quad \text{for } x = \mathrm{p},\ \mathrm{m},\quad \mathrm{b},\quad \mathrm{tm} \tag{3.3}$$

where the respective parent phase volume fractions $p_x(t;T)$ are computed using Equation 3.2. Upon further heating, the solid to liquid phase transformation, introduced in **Paper C**, is modelled by linear temperature dependence of the liquid-like phase $p_\ell(T)$, cf. [46, 47, 48]:

$$p_\ell(t;T) = \frac{T - T_{\ell 0}}{T_{\ell 1} - T_{\ell 0}}, \quad T_{\ell 0} \leq T \leq T_{\ell 1} \tag{3.4}$$

where the temperatures $T_{\ell 0}$ and $T_{\ell 1}$ represent the onset of melting and the point at which a fully melted phase is achieved, respectively. These temperature levels are set below the physical melting temperature to act as a cut-off temperature in the multi-pass welding (and heating) simulations presented in **Papers C**, **D** and **E**. In case of rapid heating events, this may result in solid to liquid phase transformations without complete preceding austenitisation, which could be considered as a modelling artefact. The volume fractions of the melting parent phases, p_x, are incrementally computed as a linear decrease from the value at the onset of melting, $p_x(T_{\ell 0})$:

$$p_x(t_n;T) = p_x(t_{n-1};T) - \frac{\Delta p_\ell(t_n;T)}{z_{\Sigma x}(t_n;T)}, \quad T_{\ell 0} \leq T \leq T_{\ell 1} \tag{3.5}$$

where the variable $z_{\Sigma x}(t_n;T)$ represents the number of parent phases during the simulated melting, i.e. the number of non-zero solid phase volume fractions $p_x(T)$ at temperature

T. Figure 3.1 illustrates that this formulation ensures that all solid phases have equal melting rates, while obtaining the correct total melting rate. For comparison, the figure also demonstrates non-equal melting rates, i.e. $p_x(T) = p_x(T_{\ell 0})\,(1 - p_\ell(T))$. This concept was disregarded as it led to prolonged states of small volume fractions, which caused convergence issues for some homogenisation methods (introduced in Section 3.3).

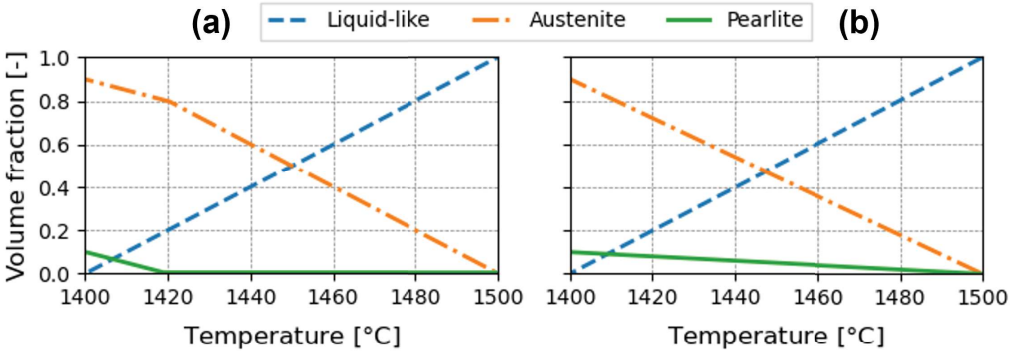

Figure 3.1: *Volume fractions during the simulated melting process using (a) equal melting rates and (b) non-equal melting rates.*

Slow or moderate cooling rates

Equation 3.4 is also used to model the transformation from the liquid-like phase to solid austenite. Upon further cooling and under low to moderate cooling rates, austenite transforms into pearlite and/or bainite. To describe these transformations, the diffusive transformation kinetics illustrated in Figure 2.3 are modelled using the JMAK equation and Scheil's additive rule. Thus, in a fully or partially austenitic state, the volume fractions of pearlite and/or bainite increase according to:

$$p_x(t;T) = p_x(\hat{t}) + p_\mathrm{a}(\hat{t})\,\left(1 - \exp\left(-b_x(T)\,(t-\hat{t})^{n_x(T)}\right)\right) \quad \text{for } x = \mathrm{p},\ \ \mathrm{b} \tag{3.6}$$

with the JMAK equation parameters as described above and with $p_\mathrm{a}(\hat{t})$ representing the austenite volume fraction at the start of the transformation and $p_x(\hat{t})$ the initial phase fraction of the nucleating phase. The remaining austenite phase fraction, $p_\mathrm{a}(t;T)$, is computed by subtracting the sum of transformed phases from the previous austenite volume fraction, $p_\mathrm{a}(t;T)$, as follows:

$$p_\mathrm{a}(t;T) = p_\mathrm{a}(\hat{t}) - \sum_x \left(p_x(t;T) - p_x(\hat{t})\right) \quad \text{for } x = \ \mathrm{p},\ \ \mathrm{b} \tag{3.7}$$

Rapid cooling

Quenching below the martensite starting temperature T_{ms}, as shown by the (near) horizontal lines in the CCT diagrams in Figure 2.3, results in the formation of martensite from any remaining austenite. This process is diffusionless and is modelled as purely temperature-dependent using the KM equation [49] for the phase fraction of the austenite $p_{\mathrm{a}}(T)$:

$$p_{\mathrm{a}}(T) = p_{\mathrm{a}}(T_{\mathrm{ms}}) \exp(-k_\theta \, (T_{\mathrm{ms}} - T)) \tag{3.8}$$

where the parameter k_θ determines the temperature dependent increase of the martensite, and $p_{\mathrm{a}}(T_{\mathrm{ms}})$ is the decreasing volume fraction of austenite at T_{ms}. Based on the remaining austenite, the volume fraction of martensite is computed as:

$$p_{\mathrm{m}}(T) = p_{\mathrm{a}}(T_{\mathrm{ms}}) - p_{\mathrm{a}}(T) \tag{3.9}$$

It was observed that during the sudden and rapid initiation of the martensite phase, some of the homogenisation methods discussed in **Paper B** encountered difficulties with FE-solver convergence. To address this issue, a smoother evolution of very low martensite volume fractions was adopted by replacing the Koistinen-Marburger equation with a hyperbolic tangent function during the initiation of the martensite transformation, as illustrated in Figure 3.2.

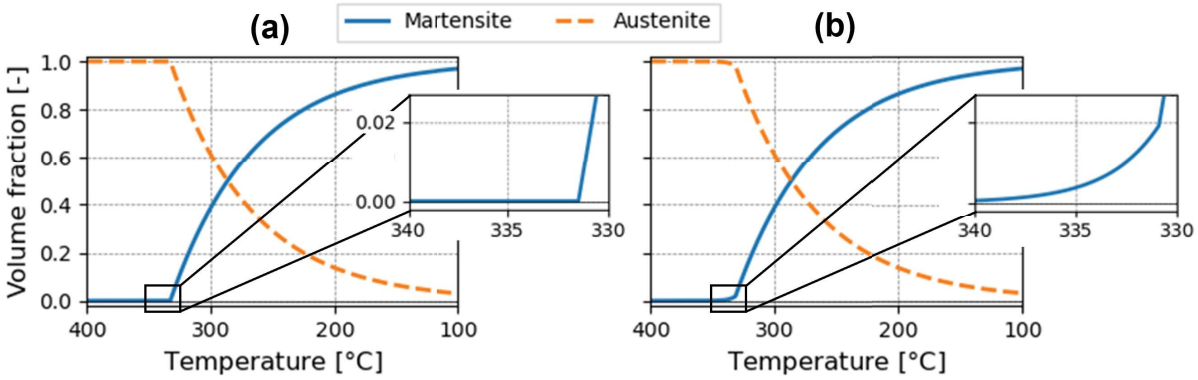

Figure 3.2: *Martensite volume fraction evolution using (a) unmodified Koistinen-Marburger equation and (b) the same equation modifed using a tangens hyperbolicus function at very low volume fractions.*

Reheating

As stated in **Paper A**, a tempered martensite phase is introduced to capture the changes in material properties and tempering stages discussed in Section 2.2. The transformation modelling is derived by replicating dilatometry experiments adopted from [50] and is assumed to be solely temperature-dependent. To capture the tempering stages, a combination of sigmoid functions is used to describe how the phase fraction of martensite, $p_{\mathrm{m}}(T)$, decreases from its initial value, $p_{\mathrm{m}}(\check{T})$:

$$p_{\mathrm{m}}(T) = p_{\mathrm{m}}(\check{T}) \left(\frac{k_1}{1 + \exp\left(k_{\theta 1}(T_{\mathrm{tm}s,1} - T)\right)} + \frac{1 - k_1}{1 + \exp\left(k_{\theta 2}(T_{\mathrm{tm}s,2} - T)\right)} \right) \tag{3.10}$$

from which the tempered martensite volume fraction, $p_{\mathrm{tm}}(T)$, is obtained as:

$$p_{\mathrm{tm}}(T) = p_{\mathrm{tm}}(\check{T}) + p_{\mathrm{m}}(\check{T}) - p_{\mathrm{m}}(T) \tag{3.11}$$

Due to difficulties in interpreting the metallographic image microscopy of the experimental procedures replicated in **Paper C**, it was decided to also model the tempering of bainite using the Equation 3.10. This assumption would be valuable to assess against experimental data in future research. The mechanical properties of tempered bainite were given those of tempered martensite, resulting in that both the martensite and bainite phases transforms into a single tempered phase. It should be noted, however, that this particular approach was not used in the repair welding simulations presented in **Paper E**.

In summary, the presented phase transformation modelling is characterised by its simplicity and versatility. It is capable of handling multi-phase material states and accounting for a wide range of temperature rates during both heating and cooling cycles, without requiring the resulting transformations to be known in advance. This facilitates large scale multi-pass weld simulations. However, it should be noted that the model does not account for stress or strain-induced phase transformations, nor the effect of microstructural grain deformation. Other alternatives found in the literature include the use of stress-conjugated extensions of the JMAK and KM equations, see e.g. [51, 52], or isothermal potential-based phase transformation functions where transformation is only triggered if it results in a decrease in the Gibbs free energy, see e.g [38, 53, 54].

3.2 Cyclic hardening plasticity

There are many methods for simulating plasticity, depending on the application and focus of the simulation. In the context of this work, which involves phenomenological modelling of the macroscopic behaviour during phase transformations, two approaches are typically used to simulate the plasticity of multi-phase material states. One approach is to use a single constitutive model with phase fractions and phase related variables as internal variables, see e.g. [55, 56]. The other approach is to use multiple mechanical models, where each phase is follows its own constitutive law, see e.g. [57, 58]. The work presented

in this thesis uses the latter approach. Furthermore, the construction of a constitutive model to simulate cyclic hardening plasticity requires the definition of a yield surface and the implementation of hardening laws, i.e. the evolution of the yield surface. For steels and other polycrystalline materials, the modelling should include the Bauschinger effect to obtain the correct yielding behaviour under reverse loading. The modelling should therefore include kinematic hardening and preferably also isotropic hardening. More detailed descriptions of the mechanical phenomena and modelling can be found in e.g. [59].

As mentioned above, the material phases introduced in the previous section are each represented by their own constitutive model. These models are identically modelled and run in parallel during simulations. Full descriptions of this constitutive model can be found in **Papers A**, **B** and **C**, but a brief description is given below. The modelling assumes small strains and that the strain components are additively decomposed as follows:

$$\boldsymbol{\epsilon}_x = \boldsymbol{\epsilon}_x^{\mathrm{e}} + \boldsymbol{\epsilon}_x^{\mathrm{th}} + \boldsymbol{\epsilon}_x^{\mathrm{tv}} + \boldsymbol{\epsilon}_x^{\mathrm{p}} + \boldsymbol{\epsilon}_x^{\mathrm{tp}} + \boldsymbol{\epsilon}_x^{\ell} \tag{3.12}$$

where total strain $\boldsymbol{\epsilon}_x$ of each individual phase x is assumed to be composed of six strain components; elastic $\boldsymbol{\epsilon}_x^{\mathrm{e}}$, thermal, $\boldsymbol{\epsilon}_x^{\mathrm{th}}$, transformation $\boldsymbol{\epsilon}_x^{\mathrm{tv}}$, plastic $\boldsymbol{\epsilon}_x^{\mathrm{p}}$, TRIP $\boldsymbol{\epsilon}_x^{\mathrm{tp}}$ and a discretized annealing strain $\boldsymbol{\epsilon}_x^{\ell}$. For simplicity, the phase specific index $\square_x$ is hereafter dropped. Moreover, linear isotropic elasticity (Hooke's law) is adopted whereby the stress, $\boldsymbol{\sigma}$, is governed by the elastic strain, $\boldsymbol{\epsilon}^{\mathrm{e}}$:

$$\boldsymbol{\sigma} = \mathbf{E}^{\mathrm{e}} : \boldsymbol{\epsilon}^{\mathrm{e}} \quad \text{with} \quad \mathbf{E}^{\mathrm{e}} = 2\,G\,\mathbf{I}_{\mathrm{dev}} + K_{\mathrm{b}}\,\boldsymbol{I} \otimes \boldsymbol{I} \tag{3.13}$$

where the fourth-order elasticity stiffness tensor $\mathbf{E}^{\mathrm{e}}$ is computed using the second-order identity tensor $\boldsymbol{I}$, the fourth-order deviatoric identity tensor $\mathbf{I}_{\mathrm{dev}}$, and the shear modulus G and bulk modulus K_{b}.

Furthermore, the modelling is implemented in FE-simulations using a strain-driven algorithm. Hence the global strain and temperature increments, $\mathrm{d}\bar{\boldsymbol{\epsilon}}$ and $\mathrm{d}T$, are given for each time increment. In combination with the multi-phase homogenisation method (discussed in Secion 3.3), these are used to calculate the elastic strain by applying Equation 3.12. In doing so, the incremental updates of the remaining five strain components are calculated using the respective governing equation and evolution law, described in short hereafter. **Paper A** introduces the computation of thermal, transformational, and plastic strains, $\boldsymbol{\epsilon}_x^{\mathrm{th}}$, $\boldsymbol{\epsilon}_x^{\mathrm{tv}}$ and $\boldsymbol{\epsilon}_x^{\mathrm{p}}$. The first two are assumed to be isotropic strains resulting from thermal expansions and changes in density during phase transformations, calculated as follows:

$$\boldsymbol{\epsilon}^{\mathrm{th}} = \alpha\,(T - \bar{T}_0)\,\boldsymbol{I}, \qquad \boldsymbol{\epsilon}^{\mathrm{tv}} = \frac{1}{3}\left(\frac{\bar{\rho}_0}{\rho} - 1\right)\boldsymbol{I} \tag{3.14}$$

where $\bar{T}_0$ and $\bar{\rho}_0$ are global, i.e. non-phase specific, material parameters for the temperature and density of the materials initial, stress free state. α and ρ are the phase-specific linear thermal expansion coefficient and the density.

The plastic strain component, $\boldsymbol{\epsilon}^{\mathrm{p}}$, is computed by adopting a Chaboche plasticity model, as proposed in e.g. [60], using the von Mises yield function and Kuhn Tucker conditions to distinguish elastic and plastic response:

$$\begin{aligned} \Phi &= \sqrt{\frac{3}{2}}|\boldsymbol{\sigma}_{\mathrm{dev}} - \boldsymbol{X}| - (R + \sigma_Y) \\ \Phi \leq 0, &\quad \dot{\lambda} \geq 0, \quad \dot{\lambda}\,\Phi = 0 \end{aligned} \tag{3.15}$$

where $\dot{\lambda}$ is the plastic multiplier. The yield function, Φ, is based on the deviatoric stress, $\boldsymbol{\sigma}_{\mathrm{dev}}$, the isotropic hardening stress R, the total kinematic hardening stress (back-stress) $\boldsymbol{X}$, and the initial yield stress σ_Y. When $\dot{\lambda} > 0$ and $\Phi = 0$, the material yields causing plastic strain and material hardening to evolve according to Equations 3.16, 3.17 and 3.18. As stated in Equation 3.16, the plastic strain evolution, $\dot{\boldsymbol{\epsilon}}^{\mathrm{p}}$, is assumed to be of associative type:

$$\dot{\boldsymbol{\epsilon}}^{\mathrm{p}} = \dot{\lambda}\frac{\partial \Phi}{\partial \boldsymbol{\sigma}} = \dot{\lambda}\sqrt{\frac{3}{2}}\frac{\boldsymbol{\sigma}_{\mathrm{dev}} - \boldsymbol{X}}{|\boldsymbol{\sigma}_{\mathrm{dev}} - \boldsymbol{X}|} \tag{3.16}$$

The total kinematic hardening stress $\boldsymbol{X}$ is obtained by summing n kinematic hardening stresses $\boldsymbol{X}_i$ following the Armstrong Frederick [61] evolution law:

$$\dot{\boldsymbol{X}} = \sum_{i=1}^{n} \dot{\boldsymbol{X}}_i = \sum_{i=1}^{n} \dot{\lambda}\,\left(\sqrt{\frac{3}{2}} C_i \frac{\boldsymbol{\sigma}_{\mathrm{dev}} - \boldsymbol{X}}{|\boldsymbol{\sigma}_{\mathrm{dev}} - \boldsymbol{X}|} - \gamma_i\,\boldsymbol{X}_i\right) \tag{3.17}$$

In addition, the evolution of isotropic hardening is adopted as follows:

$$\dot{R} = \dot{\lambda}\,b\,(R_\infty - R) \tag{3.18}$$

Other established plasticity models are available in the literature, as discussed in literature reviews by e.g. [62, 63]. In relation to the presented plasticity model, alternative approaches may involve different formulations of the yield function, as well as different kinematic and isotropic hardening laws. This can result in both other shapes and different evolutions of the yield surface. Furthermore, in addition to the presented plasticity model, other approaches may also include modelling of e.g. recovery mechanisms and viscoplastic strain rate effects. As discussed in later chapters, such modelling additions could improve the accuracy of process simulations at temperatures close to melting.

The material parameters for the presented plasticity model were calibrated by Esmaeili et al. [17] at different temperatures to fit cyclic experimental measurements and material data obtained from JmatPro [30]. The parameters for the pearlite phase were identified based on experimental results from [64], while for the martensite and tempered martensite they were identified based on experimental results from [50], and the bainite phase was modelled based on data obtained using the JmatPro software [30]. The constitutive model for the pearlite includes two back-stresses, while while for the other phases only one back-stress is included. Material parameter values are linearly interpolated and

extrapolated to cover the temperature ranges considered in this work. For the liquid-like phase introduced in **Paper C**, a nearly incompressible very soft elastic-ideal plastic solid is assumed, much like e.g. [65, 66, 67, 68].

Continuing the constitutive model summary, the TRIP strain component, $\boldsymbol{\epsilon}^{\mathrm{tp}}$ was added to the modelling in **Paper B**. This component describes the TRIP strain that arises during phase transformations under applied stress. The underlying physics is described e.g. in [69, 70, 71]. In simple terms, the expansion of the martensite phase causes significant shearing of the surrounding austenite, resulting in local plastic deformation (Greenwood-Johnson effect [69]). Furthermore, this expansion serves to alleviate stress in the austenite, resulting in an orientation effect for the growth of the martensite (Magee effect [70]). In the appended works following **Paper B**, TRIP is assumed to occur during the transformation of austenite into martensite or bainite. Therefore, only the constitutive models for these three phases include the TRIP strain component. The implementation uses the formulation proposed by [72, 37, 56] and material parameters obtained from [33] as follows:

$$\dot{\boldsymbol{\epsilon}}^{\mathrm{tp}} = \frac{3}{2} K_{\mathrm{tp}} \boldsymbol{\sigma}_{\mathrm{dev}} \frac{df(p)}{dp} \dot{p} \tag{3.19}$$

where $f(p)$ is a saturation function in which p represents the increasing volume fraction of the phase transformation, described in further detail in **Paper B**. It is important to note that the material parameter values for the TRIP strain adopted in the appended papers are not for ER7 wheel steel or R260 rail steel. As parameter values for these steels are not readily available, the values used are from a low-alloy tool steel [33], with phase transformation kinetics similar to the wheel steel and a carbon equivalent similar to the rail steel. For this reason, the TRIP strain computation for all three phases used the same parameter values. Experimental work to obtain more accurate parameter values would be valuable improvements in future research. Moreover, it should be noted that in order for the material model to obtain the correct homogenised TRIP effect, **Paper B** shows how the TRIP strain component had to be implemented not only in the nucleating phase but also in the decreasing austenite parent phase.

Furthermore, in **Paper C** the annealing strain component, $\boldsymbol{\epsilon}^{\ell}$, was introduced. This was done to impose a zero-stress state at high temperatures and, in particular, to obtain a virgin material at solidification. It was introduced as follows:

$$\begin{cases} \boldsymbol{\epsilon}^{\ell} = -\left(\boldsymbol{\epsilon}^{\mathrm{th}} + \boldsymbol{\epsilon}^{\mathrm{tv}} + \boldsymbol{\epsilon}^{\mathrm{p}} + \boldsymbol{\epsilon}^{\mathrm{tp}} - \boldsymbol{\epsilon}\right), & \text{if } p_{\ell} = 1 \\ \dot{\boldsymbol{\epsilon}}^{\ell} = 0, & \text{if } p_{\ell} \neq 1 \end{cases} \tag{3.20}$$

It is well established that modelling the recovery of a virgin material state during melting and solidification is important in welding simulations, see e.g. [73]. To achieve this, the annealing strain component $\boldsymbol{\epsilon}^{\ell}$ is fixed at the onset of solidification while simultaneously resetting the internal state variables such as plastic strains and hardening variables. This ensures that solidification starts from a stress-free, virgin material state. In addition, to achieve realistic thermal contraction of the previously melted material, the reference

temperature and density, $\bar{T}_0$ and $\bar{\rho}_0$, for the thermal and transformation strains, $\boldsymbol{\epsilon}^{\text{th}}$ and $\boldsymbol{\epsilon}^{\text{tv}}$ in Equation 3.14, are reset upon completed solidification such that $\bar{T}_0 = T_{\ell 0}$ and $\bar{\rho}_0 = \rho_{\text{a}}$. Experimental comparisons presented in **Paper D** confirm that the thermal contraction behaviour is realistically modelled. Furthermore, this modelling assures the preservation of total strain for each constitutive model while resetting the internal state variables of all solid phases without affecting the stability of the numerical finite element solver. This approach is similar to that proposed by [74].

In literature, it is generally accepted that using a mixed hardening plasticity model, including the TRIP effect, and modelling of virgin material recovery are all important aspects for accurate welding simulations. However, there are a plethora of phenomenological and macroscopic alternatives available for modelling these aspects. For instance, flow stress modelling in welding simulations can be achieved using dislocation density based plasticity models and elastic-viscoplastic models, as demonstrated in e.g. [75] and [76]. These references also highlight the significance of stress relaxation, a feature that the presented modelling does not include. Furthermore, some alternative formulations for modelling TRIP strain in welding simulations do not require additional material parameters, but instead use the specific volume change and yield stress of the material phases, see e.g [77, 78]. With regard to the recovery of the initial virgin material condition, the recovery (or annealing) process presented in this work is somewhat ad hoc and is enabled by the parallel individual phase constitutive models. However, there are numerous examples in the literature where annealing has been modelled by simply resetting the plastic strain and hardening, see e.g. [79, 80]. On the other end, more complex temperature-driven evolution laws for material recovery can also be found, see e.g. [81].

3.3 Multi-phase homogenisation methods

When modelling a multi-phase material state, the global constitutive behaviour can be obtained by homogenising the behaviour of the individual phases, see e.g. [82, 33]. The most common homogenisation method for phase transformation simulations found in the literature is the linear mixture rule, see e.g. [32, 37]. However, examples of non-linear mixture rules can also be found. For instance, in [83, 84], it is shown that linear mixture rules may not be sufficient to replicate experimental material behaviour.

In **Paper A** an isostrain homogenisation method is used and in **Paper B** three additional methods are used: isostress, a self-consistent model, and the linear mixture rule, and the performance of all four methods is compared and evaluated. This brief summary will begin with the linear mixture rule, which is the most straightforward method as it does not require individual material models for the phases, see e.g. [20, 37]. The method computes the material model parameter values by taking the phase volume fraction scaled average. For instance, the initial yield stress $\bar{\sigma}_y$ is calculated as follows:

$$\bar{\sigma}_y = \sum_x p_x \sigma_{y,x} \quad \text{for } x = \text{a}, \quad \text{p}, \quad \text{b}, \quad \text{m}, \quad \text{tm}, \quad \ell \tag{3.21}$$

During each time increment, it is assumed that the temperature and phase volume fractions remain constant. For the isostrain, isostress and self-consistent homogenisation methods, this assumption allows for the homogenised strain and stress to be computed from the phase volume fraction scaled averages of the individual strains and stresses as follows:

$$\mathrm{d}\bar{\boldsymbol{\epsilon}} = \sum_x p_x \, \mathrm{d}\boldsymbol{\epsilon}_x \qquad \mathrm{d}\bar{\boldsymbol{\sigma}} = \sum_x p_x \, \mathrm{d}\boldsymbol{\sigma}_x \tag{3.22}$$

The isotrain homogenisation method assumes that all phases have the same strain increment, i.e. $\mathrm{d}\boldsymbol{\epsilon}_x = \mathrm{d}\bar{\boldsymbol{\epsilon}}$. Therefore, the homogenised stress increment can be obtained using the following formula:

$$\mathrm{d}\overline{\boldsymbol{\sigma}} = \sum_x p_x \, \mathbf{E}_x : \left(\mathrm{d}\boldsymbol{\epsilon}_x - \mathrm{d}\boldsymbol{\epsilon}_x^{\mathsf{th}} - \mathrm{d}\boldsymbol{\epsilon}_x^{\mathsf{tv}}\right) = \sum_x p_x \, \mathbf{E}_x : \left(\mathrm{d}\bar{\boldsymbol{\epsilon}} - \mathrm{d}\boldsymbol{\epsilon}_x^{\mathsf{th}} - \mathrm{d}\boldsymbol{\epsilon}_x^{\mathsf{tv}}\right) \tag{3.23}$$

where $\mathbf{E}_x$ represents the tangent stiffness. In contrast, the isostress homogenisation method assumes that all phases experience the same stress increment, i.e. $\mathrm{d}\boldsymbol{\sigma}_x = \mathrm{d}\overline{\boldsymbol{\sigma}}$. Hence, the homogenised strain increment can be obtained as follows:

$$\mathrm{d}\bar{\boldsymbol{\epsilon}} = \sum_x p_x \, \left(\mathbf{E}_x^{-1} : \mathrm{d}\bar{\boldsymbol{\sigma}} + \mathrm{d}\boldsymbol{\epsilon}_x^{\mathsf{th}} + \mathrm{d}\boldsymbol{\epsilon}_x^{\mathsf{tv}}\right) \tag{3.24}$$

However, in a strain increment-driven finite element algorithm, the stress increment $\mathrm{d}\bar{\boldsymbol{\sigma}}$ is unknown. Therefore, an additional Newton iteration scheme is used to calculate the individual phase strain increments $\mathrm{d}\boldsymbol{\epsilon}_x$ to satisfy both the isostress assumption and the homogenised strain increment (Equation 3.22).

The isostrain and isostress homogenisation methods provide theoretical upper and lower bounds for elastic material response. Between these bounds, a physically motivated alternative is the self-consistent homogenisation method. Based on Eshelby's inclusion theory [85], this method assumes each phase to be an inclusion in the surrounding body of homogenised state. As such, the stress, strain, and displacement fields of each phase are affected by the homogenised state, of which itself is a contributing part. Originally formulated for elasticity, the method is extended to plasticity by [86]. Unlike the isostrain and isostress methods, this method does not prescribe the strain or stress increments. Instead, the strain increment for each phase $\mathrm{d}\boldsymbol{\epsilon}_x$ is computed as follows:

$$\mathrm{d}\boldsymbol{\epsilon}_x = \mathbf{A}_x : \mathrm{d}\bar{\boldsymbol{\epsilon}} \tag{3.25}$$

where the fourth order concentration tensor $\mathbf{A}_x$ is iteratively computed based on the Eshelby tensor, see e.g. [87], in a fixed-point iteration procedure at the start of each time increment. This pre-processing procedure uses the individual phase tangent stiffnesses $\mathbf{E}_x$ from the previous time increment to compute the current time increment concentration tensors $\mathbf{A}_x$, described in further detail in **Paper B**. The homogenised stress increment is then computed similarly to the isostrain method (see Equation 3.23):

$$\mathrm{d}\overline{\boldsymbol{\sigma}} = \sum_x p_x \, \mathbf{E}_x : \left(\mathrm{d}\boldsymbol{\epsilon}_x - \mathrm{d}\boldsymbol{\epsilon}_x^{\mathsf{th}} - \mathrm{d}\boldsymbol{\epsilon}_x^{\mathsf{tv}}\right) = \sum_x p_x \, \mathbf{E}_x : \left(\mathbf{A}_x : \mathrm{d}\bar{\boldsymbol{\epsilon}} - \mathrm{d}\boldsymbol{\epsilon}_x^{\mathsf{th}} - \mathrm{d}\boldsymbol{\epsilon}_x^{\mathsf{tv}}\right) \tag{3.26}$$

Unlike the isostrain method, both the isostress and self-consistent homogenisation methods require additional computational steps to obtain each phase's individual strain increments. Of these additional steps, the algorithm of the self-consistent method is less computationally expensive and more numerically stable. **Papers B** and **C** demonstrate that this method also produces more physically realistic behaviour during the multi-phase stages of the welding process. This is achieved by not stringently imposing the stress or strain state of the parent phase onto the nucleation phase. As a result, a softer parent phase can undergo plastic deformation while a stiffer nucleating phase exhibits elastic behaviour. Another often used analytically based homogenisation method with this capability is the isowork homogenisation method, which assumes that all individual phases perform the same internal work, see e.g. [88, 84]. However, this method requires an additional Newtonian iteration scheme, similar to the isostress method, to obtain the individual strain increments such that the isowork condition is satisfied.

In contrast to linear mixture rules or analytically based homogenisation techniques, a third option for homogenisation is to use an FE description of either a unit cell or a representative microstructure in multi-scale simulations. Although potentially more accurate, this approach is significantly more complex and computationally expensive, particularly for transient simulations. Consequently, transient 3D macroscale welding simulations using this method are rare. Comparable examples are limited but include mesoscale transient simulations that consider hot cracking phenomena [89] and post-weld (as-welded) low-cycle fatigue simulations [90].

3.4 Material modelling demonstration

The thermo-metallurgical-mechanical behaviour of the material model presented in previous sections is here demonstrated using a conceptual 3-bar welding simulation, described in **Paper C**. The material model is implemented as user-defined subroutines in the commercial FEM software Abaqus [91]. Figure 3.3 shows the model used in the FE-simulation, with the heated bar in the centre and the two cold bars on either side. The cold bars are five times wider than the heated bar. In the model, the centre bar is heated by prescribing its nodal temperatures while constraining its axial expansion by rigidly connecting the free end of the bar to the ends of the cold bars. This set-up estimates the longitudinal stress component in a butt weld fusing two large plates.

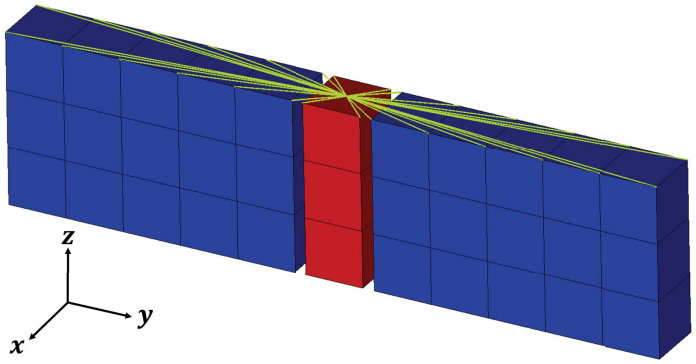

Figure 3.3: *3-bar FE-model, with the heated centre bar highlighted in red and the five times wider cold bars on either side. The bars are connected via a rigid coupling highlighted by thin green lines at the top of the bars.*

Figure 3.4 presents the simulation results of the conceptual 3-bar welding simulation. The top graph shows the prescribed temperature of the heated bar. Three 10 second heating cycles from 20 to 1600°C are simulated, with the final heating cycle having a slower, 30 second cooling cycle. This temperature load results in the phase transformations and multi-phase states demonstrated by the volume fractions in the second graph. The third graph shows how, as discussed in **Paper C**, the homogenisation methods produce significantly different stresses during the phase transformations, with the self-consistent method considered to produce the most physically realistic material response. The graph also illustrates the virgin material state achieved in each melting and remelting cycle, where the material response is repeated in each subsequent cooling and reheating cycle.

The fourth graph in Figure 3.4 illustrates the stress obtained using the self-consistent homogenisation method with various modelling features turned off. This demonstrates the significant influence of the modelling features. Specifically, it highlights how the influence of a particular feature can be small at one time instance but significant at another. An example of this is how, for the simulated temperature load, the stress obtained with and without the virgin material annealing feature happens to become similar at the final time instance, while differing at other time instances. Moreover, running the simulation with elastic material phases or without phase transformations results in an unrealistic material response, as expected. However, it is important to note that simulations without the modelling features could produce more accurate results if the material parameters are tuned differently, e.g adjusting the yield stress to account for high-temperature softening or to simulate TRIP effects.

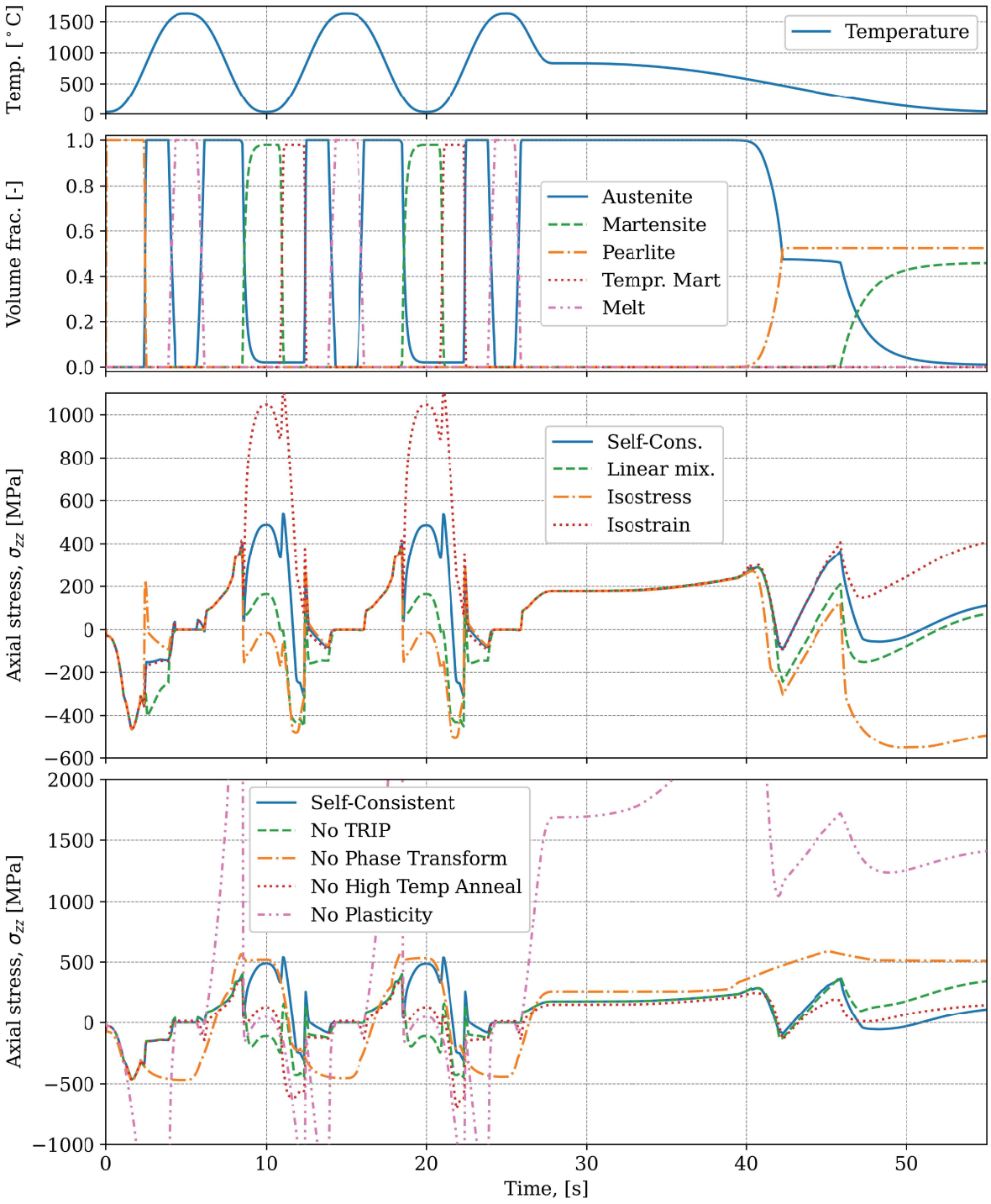

Figure 3.4: *Temperature load and simulation results for the 3-bar welding simulation shown in Figure 3.3. Top graph: temperature load. Second graph: phase transformations and volume fractions. Third graph: Longitudinal stress obtained by different homogenisation methods. Fourth graph: Longitudinal stress obtained without modelling features.*

4 Computational mechanics in high temperature processes

4.1 Thermo-metallurgical-mechanical finite element framework

High temperature operations in steels involve simultaneous thermal, mechanical and metallurgical processes occurring on different time and length scales, as discussed in Chapter 2. Most of aspects these processes can be accounted for using FEM, some of them are described in Chapter 3. Figure 4.1 provides a schematic view of the couplings between the thermal, mechanical and metallurgical processes, which have been described in more detail by e.g. [57, 92]. Certain simplifications of these interacting couplings can be made without significantly compromising the accuracy of the simulation results, as shown by e.g [93, 94]. In line with the scope of the present work, this motivates the adopted strategy of decoupling the thermo-metallurgical-mechanical analysis into a transient thermal analysis, followed by a quasi-static mechanical analysis. The temperature field history obtained from the thermal analysis drives the metallurgical processes described in Sections 2.2 and 3.1. The combined effect of these processes, together with any additional mechanical loading, then determines the mechanical response of the material. Figure 4.1 illustrates these coupling phenomena, with the black and grey arrows indicating included and excluded coupling phenomena, respectively. In reference to Chapter §3, the corresponding strain components are $\boldsymbol{\epsilon}^{\mathrm{th}}$, $\boldsymbol{\epsilon}^{\mathrm{tv}}$, $\boldsymbol{\epsilon}^{\mathrm{tp}}$ and $\boldsymbol{\epsilon}^{\ell}$. Moreover, the adopted quasi-static assumption of the mechanical analysis is widely accepted due to the negligible inertia effects in fusion welding processes [95].

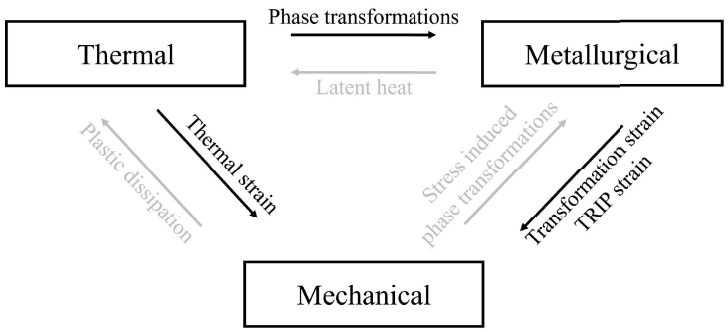

Figure 4.1: *Coupling mechanisms between thermal field, microstructure evolution and mechanical field in the applied thermo-metallurgical-mechanical simulation methodology. Mechanisms written in black text are considered, while mechanisms written in grey text are not considered in this work.*

In this simplified modelling framework, the exclusion of latent heat is believed to have the greatest impact on the accuracy of the simulation, according to the literature, e.g. [96]. However, several authors, e.g. [97, 98], have effectively applied this simplification by claiming that the influence in welding applications is negligible, likely owing to the substantial local heat input inherent in welding processes. This also justifies the assumption that the influence of the plastic dissipation is negligible compared to the welding heat input and that the deformations are small enough not to affect the geometry, and therefore, neither the thermal boundary conditions. Moreover, the final simplification assumes that the stress field does not affect the microstructure evolution, i.e. excluding stress-induced phase transformations and the Magee TRIP effect [70]. This is largely a micromechanical effect and therefore out of scope for the scales of mechanical problems considered in the present work. It is worth noting that many of the more detailed alternative modelling approaches briefly mentioned in Chapter 3 would not allow for the decoupling or one-way interaction simplifications presented here.

4.2 Local heating events

Concentrated localised heating on the wheel tread and rail surface is detrimental to the mechanical performance of the wheel-rail contact interface, as documented in wheel-rail thermal loading reviews by e.g. [99, 100]. Elevated temperatures, caused by intense frictional heat generated during train wheel brake lock-up or inadequate traction during acceleration, can induce austenitisation in the sliding contact interface. Subsequent rapid heat dissipation results in martensite formation, leading to stress concentrations and heterogeneous, brittle material properties. These phenomena are known as wheel flats on the wheel tread and wheel burns on the rail surface, and significantly contribute to rolling contact fatigue. Numerical simulations of wheel flats are relatively rare in the literature, see e.g. [18, 101], and simulations of the corresponding wheel burn induced rail surface damage are even less common, see e.g. [102, 103]. **Papers A** and **B** utilise the presented modelling framework to simulate events related to these occurrences. **Paper A** investigates a double wheel flat scenario on a railway wheel, simulating the repeated occurrence of wheel skidding at the same location, as illustrated in Figure 4.2. **Paper B** replicates an experimental procedure, see [104], using focused laser heating on the railhead surface, as depicted in Figure 4.3.

Figures 4.2b and 4.3c show the 2D axisymmetric FE models used in **Papers A** and **B** for thermal and mechanical simulations. Both studies apply uniform heat flux to a segment of the model surface and, importantly, demonstrate the modelling framework's capability to simulate the resulting phase transformations. In addition, **Paper A** uses a 3D simulation of the same heating event and investigates how residual stresses are influenced by subsequent cyclic mechanical loading. Figure 4.2 demonstrates that the simulated phase transformations of the double wheel flat, as presented in **Paper A**, closely

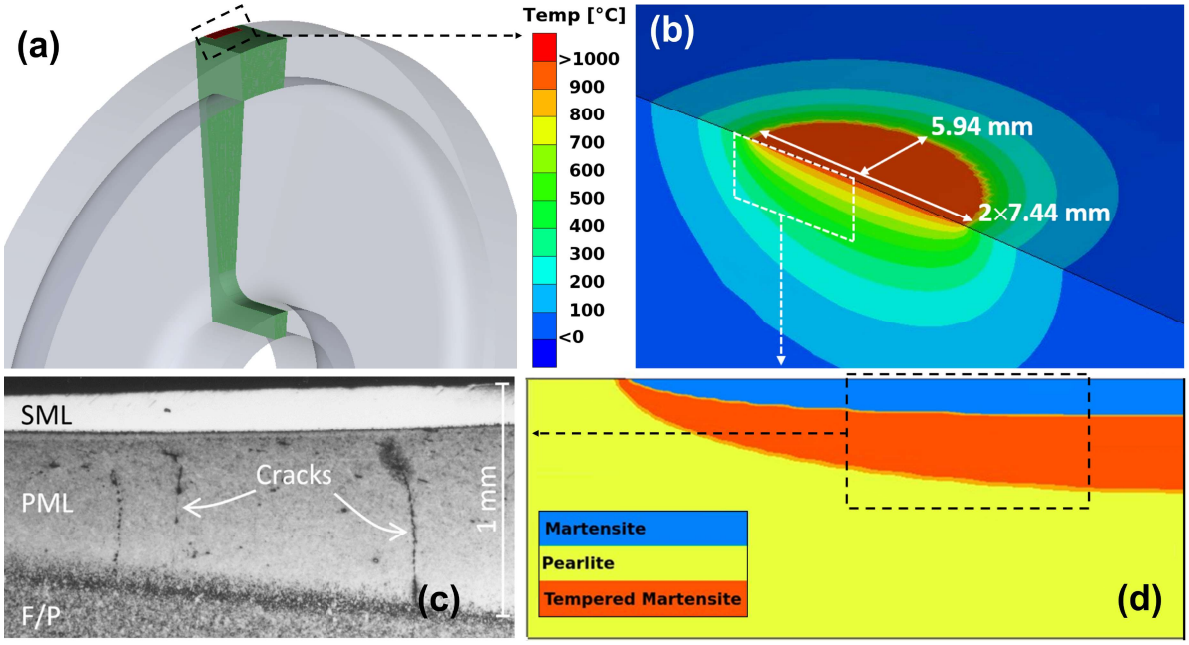

Figure 4.2: *Double wheel flat simulation presented in* ***Paper A****. (a) 3D illustration of half the wheel. (b) temperature field resulting from the applied surface heat flux. (c) image metallographic microscopy from Ahlström et. al. [105]. (d) predicted phases.*

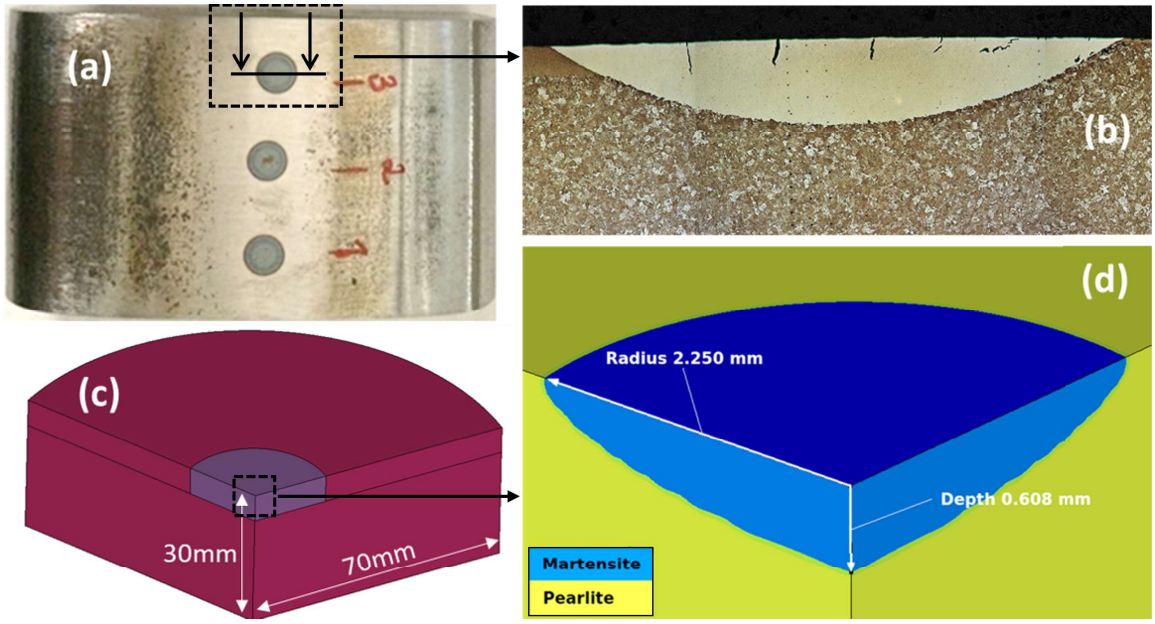

Figure 4.3: *Rail surface laser heating presented in* ***Paper B****. (a) rail sample used experimental procedure by Jessop et. al [104] and (b) corresponding metallographic microscopy. (c) illustration of 2D axi-symmetric FE model. (d) predicted material phases resulting from the applied surface heat flux.*

align with experimental results in [15]. Similarly, the rail surface laser heating simulation presented in **Paper B** and shown in Figure 4.3 shows a good correlation between the simulated and experimentally observed phase transformations.

The resulting residual stress fields from heating on the wheel and rail surface are presented in Figures 4.4a and 4.4b. The stress plots combined with the volume fraction plots shown in Figures 4.2d and 4.3d offers valuable insights for evaluating the risk of subsurface cracking in the HAZ of the wheel and rail. **Paper B** also compares the simulated residual surface stresses to experimental measurements, as shown in Figure 4.5. Specifically, the figure compares the residual stresses obtained using different homogenisation methods. Although the results are of the same order of magnitude and the overall trend is valid, none of the homogenisation methods gives a perfect match. Moreover, only minor differences between the methods were observed due to the short duration of the multi-phase stages. However, in the narrow multi-phase region a the 2 mm radius mark in Figure 4.5, the homogenisation methods differ significantly. It is worth noting that the modelling at this stage did not include the liquid-like phase and the discretised annealing strain component later introduced in **Paper C**. Rerunning the simulation with these updates (using the self-consistent homogenisation method) improves the experimental correlation, as shown in Figure 4.5. As a qualitative validation, the updated simulation model correlates better with the surface micro cracks shown in Figure 4.3b, as it predicts somewhat higher tensile surface stresses. However, it is important to note that the correlation between experimental and simulation results is not as strong as presented in **Paper D**. This emphasises the value of the simulation methodology used in **Papers C**, **D** and **E**, which will be presented in Section 4.3.3.

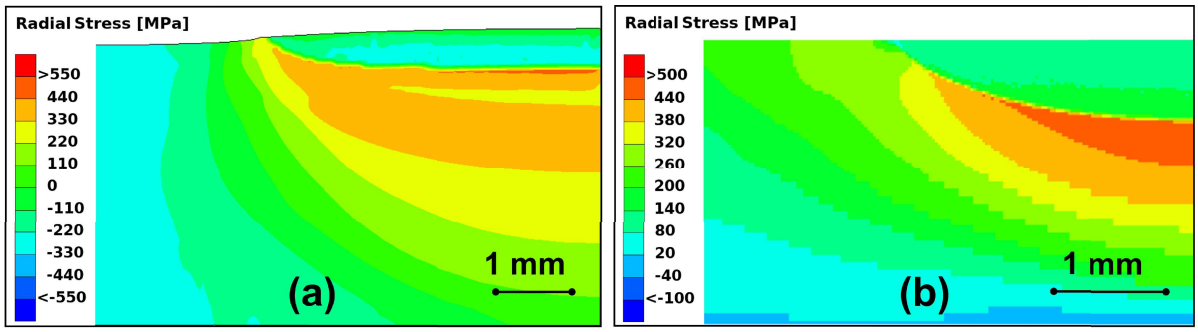

Figure 4.4: *Residual stress fields (radial stress component in axi-symmetric FE model) resulting from the simulated surface heating events. (a) Wheel flat simulation from* ***Paper A****, illustrated in Figure 4.2. (b) Rail surface laser heating simulation from* ***Paper B****, illustrated in Figure 4.3.*

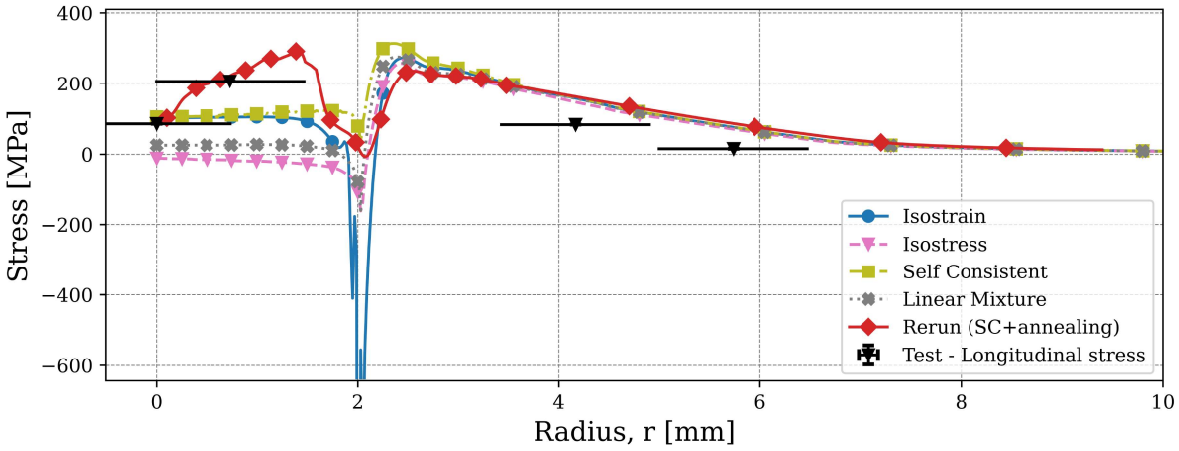

Figure 4.5: *Comparison of simulated radial surface residual stress, obtained using different homogenisation methods, and experimental measurements from Jessop et. al [104]. The simulation is performed in* ***Paper B****, and illustrated in Figure 4.3. Rerun simulation results uses the material model improvements presented in* ***Paper C***

4.3 Welding

As mentioned in the previous sections, welding is an inherently complex, multi-physics and multi-scale transient process that requires the consideration of several overlapping physical phenomena in simulations. Modelling of numerous interacting phenomena in wire arc welding is highlighted in the review article [106]. Fortunately, many of these interactions prove to be negligible compared to what Lindgren [95] refers to as classical computational welding mechanics (CWM), which only includes the interactions shown in Figure 4.1. However, depending on the scope of the analysis, additional interactions may need to be included. For example, the heat source model may require the inclusion of arc physics, see e.g. [107, 108], while a focus on mechanical and metallurgical interactions may require considerations such as grain growth, see e.g. [109, 110], or alloy precipitation, see e.g. [111, 112]. These processes affect the residual state of the material and influence properties such as hardness, strength and toughness. However, in macroscopic welding simulations it is primarily the phase transformation aspect that is most often considered, the influence of which is illustrated by the 3-bar example presented in Figure 3.4.

To apply the macroscopic modelling framework of **Papers A** and **B** in multi-pass repair welding simulations following typical CWM principles, **Paper C** introduces models for both the heat source and the filler material.

4.3.1 Heat source modelling

3D welding heat transfer simulations typically require the modelling of the moving heat source in the wire arc welding process. Two common techniques found in the literature

are either the use of prescribed nodal temperatures, see e.g. [113, 114], or the use of prescribed heat flux, see e.g. [98, 115, 116]. Modelling of the actual arc physics is a complex area of research, although it is possible, see e.g. [117], it is not required at the detail level considered in this thesis. In **Papers C**, **D** and **E** the technique with a prescribed heat flux is adopted.

To model the heat flux from the welding arc, several heat distribution shapes have been proposed in the literature. Common choices are the Gaussian distribution, see e.g. [118], a double ellipsoid distribution, see e.g. [119, 120], and a conical distribution, see e.g. et al. [121]. In [122], results of the three distributions are compared and it is shown that all give valid predictions of the temperature field, with the latter two giving very similar results. For high fidelity predictions of the fusion zone, intricate combinations of heat flux distributions may be advantageous, see e.g. [123]. The simulations of manual arc welding in **Papers C** and **E** adopt a double ellipsoid heat distribution, while the simulation of laser weld heating in **Paper D** adopts a Gaussian heat distribution, as shown in Figures 4.6a and 4.6b. These are implemented in Abaqus [91] as user-defined subroutines and also include a cut-off temperature.

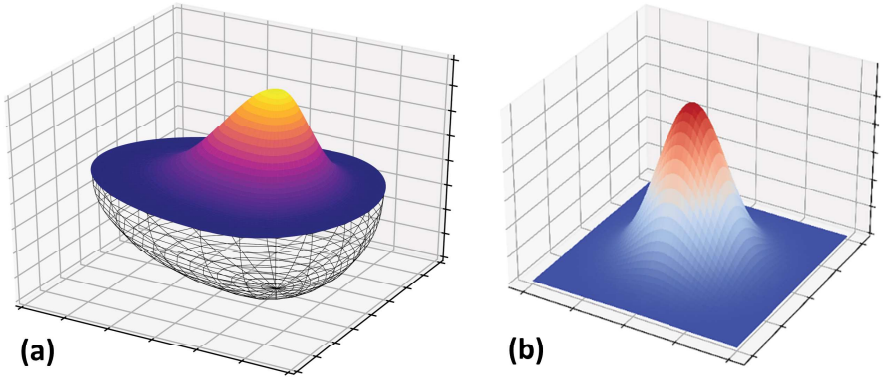

Figure 4.6: *Generic illustrations of (a) a double ellipsoid heat source used in **Papers C** and **E** and (b) a Gaussian heat distribution used in **Paper D**.*

In CWM, it is widely acknowledged that the accuracy of the heat input modelling significantly influences the fidelity of simulation outcomes, see e.g. [124, 125, 126]. This can also be understood from Figure 4.1, as the applied heat flux dictates the temperature field and thus indirectly the mechanical and metallurgical simulation outcome. To address this crucial aspect, the heat source modelling in **Papers D** and **E** is carefully tuned by comparing simulation results to experimental measurements demonstrated in Figures 4.7 and 4.8, respectively. In the tuning procedures, the power of the welding machine and the traversing speed of the weld torch are known. Therefore, the tuning is focused on adjusting the spatial distribution parameters of the heat sources and the heat source cut-off temperature. These parameters are manually adjusted such that the simulated regions undergoing phase transformations match surface hardness and metallographic and cross-sectional hardness measurements.

A similar approach is adopted in the welding simulations presented in **Paper C**. However, this study replicates an experimental process from the literature [127, 128] and could not be tuned as precisely due to the lack of data. A more accurate and less ambiguous method for adjusting the heat source would be to calibrate using transient temperature measurements, see e.g. [129, 130]. Unfortunately, no such measurements were available for the work presented in the appended papers.

Moreover, the complexity of accurately modelling the heat source is emphasised by the metallographic study of HAZs presented in **Paper D**. The study demonstrated that, in certain cases, a significant difference in effective heat input had only a minor impact on the resulting phase transformed region. This highlights the importance of knowing process parameters, such as the input power and torch speed of the welding machine.

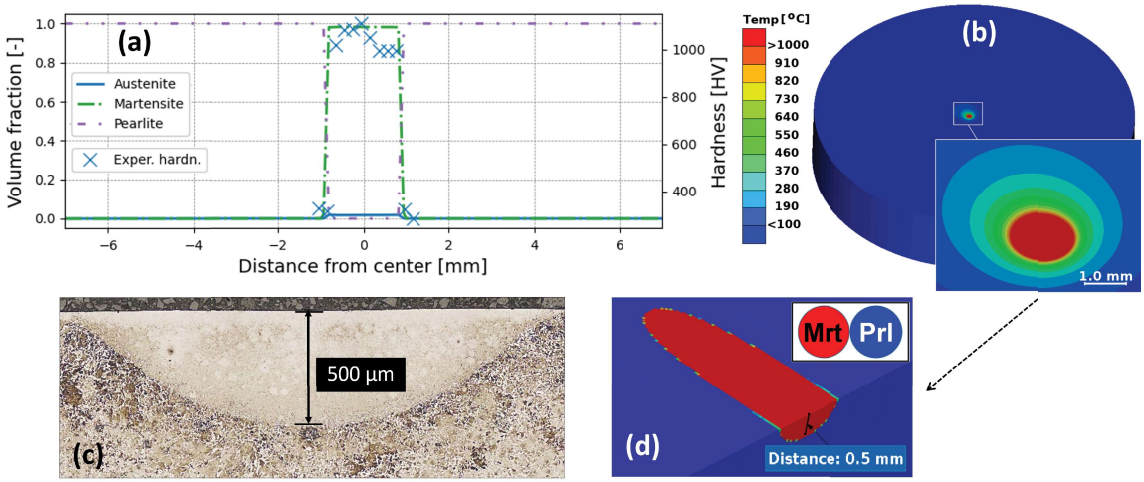

Figure 4.7: *Calibration of heat source used in simulations presented in* ***Paper D****. (a) surface hardness measurement and simulate material phases. (b) simulated temperature field. (c) microscopic metallographic image of martensitic band. (d) simulated martensitic band on the material sample surface.*

4.3.2 Filler material modelling

In wire arc welding, filler material is continuously added during the welding process and the applied heat melts both the filler and the base material, fusing the two components together. To accurately simulate this process using FEM, the simulation model must be able to handle elements that are continuously added during the simulation. Two common approaches to this modelling challenge can be found in the literature; the quiet (or silent) element technique, see e.g. [113, 131, 132], and the element birth (or inactive) technique, see e.g. [129, 133, 134]. Comparative studies, by e.g. [135], show that both methods produce similar temperature and stress fields in thermal and mechanical simulations. However, the quiet element approach is more conveniently implemented in the software

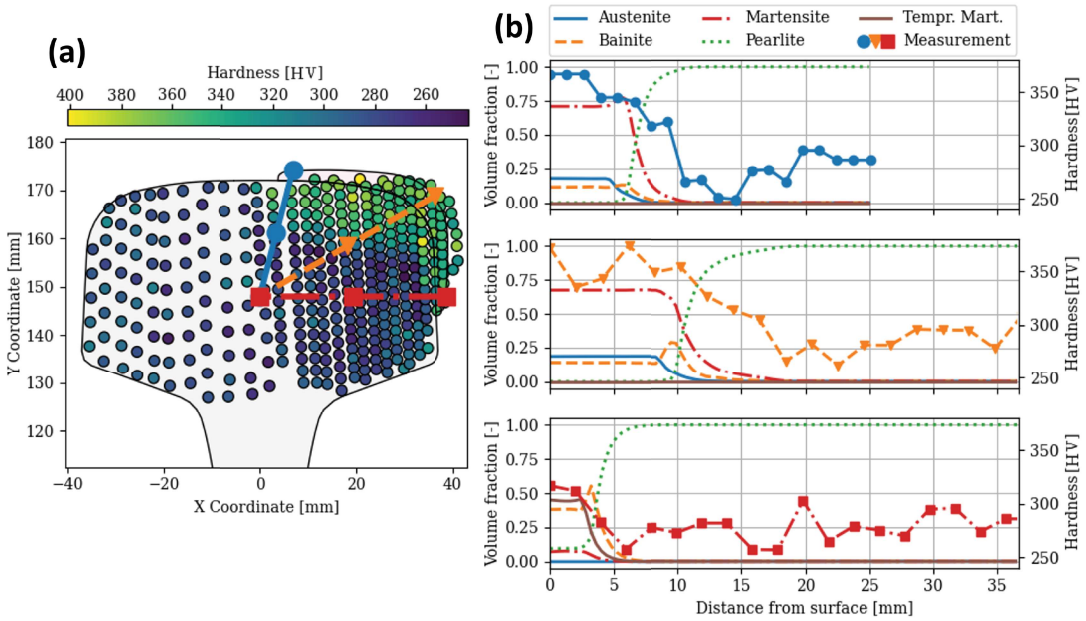

Figure 4.8: *Calibration of heat source used in simulations presented in* ***Paper E****. (a) surface hardness measurements and plot paths used in simulation calibration. (b) three graphs showing hardness measurements and simulate material phases plotted along the respective colour highlighted plot path.*

used in this study (Abaqus) and can be easily incorporated into the multi-phase modelling described in Section 3.2, and is therefore the preferred method in the presented work.

In the thermal simulations, the quiet elements, representing the non-activated filler elements, are given a low thermal conductivity and an initial temperature equal to the cut-off temperature of the heat source. When activated by the moving weld torch, they are given regular thermal properties allowing them to absorb heat flux from the heat source and to participate in heat transfer. To avoid fictitious temperature gradients between the filler and base material elements, these elements do not share nodes. Instead, the interface is connected by a conduction contact that is activated at the same time as the quiet elements, similar to the gap conduction elements used by e.g.[136].

For the mechanical simulations, the quiet state of the filler elements is achieved by assigning these elements the liquid-like phase. The mechanical properties of these elements are then such that they do not influence their neighbouring activated elements. During the solidification process, the annealing strain component removes the effect of any strain accumulated in the quiet state, similar to the proposal in [74]. Similar to the FE mesh of the heat transfer simulation, the filler elements do not share nodes with the base material and tie constraints are used to permanently connect the surfaces. The nodal positions of the filler elements are not adjusted upon element activation as in e.g. [137, 138]. This simplification is valid if the deformations are small, which is assumed in the modelling presented in Section 3.2.

4.3.3 Methods for improved computational efficiency

When simulating the welding process, careful consideration must be given to which and how to include the various overlapping multi-physics and multi-scale phenomena discussed in Section 4.1. Computational modelling of these interacting phenomena is computationally expensive and requires good knowledge of both material characteristics and process parameters. Despite incorporating conventional CWM simplifications, as shown in Figure 4.1, the computational time and amount of input data required to simulate a full-scale 3D multi-pass welding process are often beyond the practical limits for the modelling to be a useful engineering tool. This computational challenge underscores the need to explore innovative methods that balance computational efficiency with accurate representations of the inherent complexities of welding.

Using a coarser mesh to save computational cost is often not a viable option as a dense mesh is required to accurately predict thermal gradients and thereby resolve stress gradients in critical areas such as the fusion zone. A dense mesh also reduces the effects of inconsistent continuity of the total and thermal stress fields, see e.g [139, 140, 141]. A computationally efficient way to obtain a dense mesh in the moving HAZ while having a coarse mesh in the far-field regions is to use an adaptive mesh scheme, see e.g. [142, 143]. Using combinations of shell and solid elements in the FE mesh is another way to gain efficiency, see e.g. [144, 145, 146]. An alternative method to enable larger time steps in the simulations is to not add or activate the filler elements one by one, but to lump them into larger segments, so called macro beads, cf. [147], and activate them simultaneously, see e.g. [148, 138]. When simulating multi-pass welding scenarios, it is also common to lump multiple passes or layers together, see e.g [149, 150]. It should be noted that although many of the mentioned discretisation techniques date back decades, they remain highly relevant in modern applications such as additive manufacturing simulations, see e.g. [151, 152].

As explained above, the computational cost is to some extent cumulative when different thermo-metallurgical-mechanical phenomena are included in the transient weld analysis. One remedy is not to simulate these interactions explicitly, but instead use the inherent strain method. In this method, an a priori determined strain tensor, containing the plastic, thermal, creep and transformation strains resulting from the welding process, is imposed on the elements of the HAZ during the simulated welding process, see e.g. [153, 154]. Although this method is computationally efficient, some disadvantages are that all details of the welding conditions may not be fully accounted for and deriving the inherent strain tensor is not a trivial task.

The use of FE model reduction or sub-model techniques is another way to improve computational efficiency without necessarily omitting thermo-metallurgical-mechanical phenomena. The simplest and most commonly used model reduction is the use of 2D simulations. For structures that are geometrically uniform in the weld direction, 2D simulations have been shown to reproduce 3D simulations and experimental measurements

with acceptable accuracy, see e.g. [155, 156, 157]. A similar approach is adopted in the simulation methodology developed in **Paper C**. As will be described in Section 5.2, this methodology takes advantage of the longitudinal uniformity of the rail by combining a less computationally expensive, full scale 3D heat transfer simulation with a computationally efficient 2D mechanical simulation. Although more sophisticated model reduction schemes can be found, e.g. in [158], **Papers C** and **D** show that the 2D model simulation results correlate reasonably well with experimental measurements and reproduces the results obtained using a 3D mechanical simulation model, as shown in Figure 4.9. The figure compares stress histories at two points in the rail repair procedure presented **Paper C** (Figures 4.9a and 4.9b), and surface residual stresses from laser heating simulations, as presented in **Paper D** (Figure 4.9d). Importantly, this modelling allows for full utilisation of the material modelling presented Chapter 3 at a fraction of the corresponding complete 3D model simulation time, as demonstrated in Figure 4.9c.

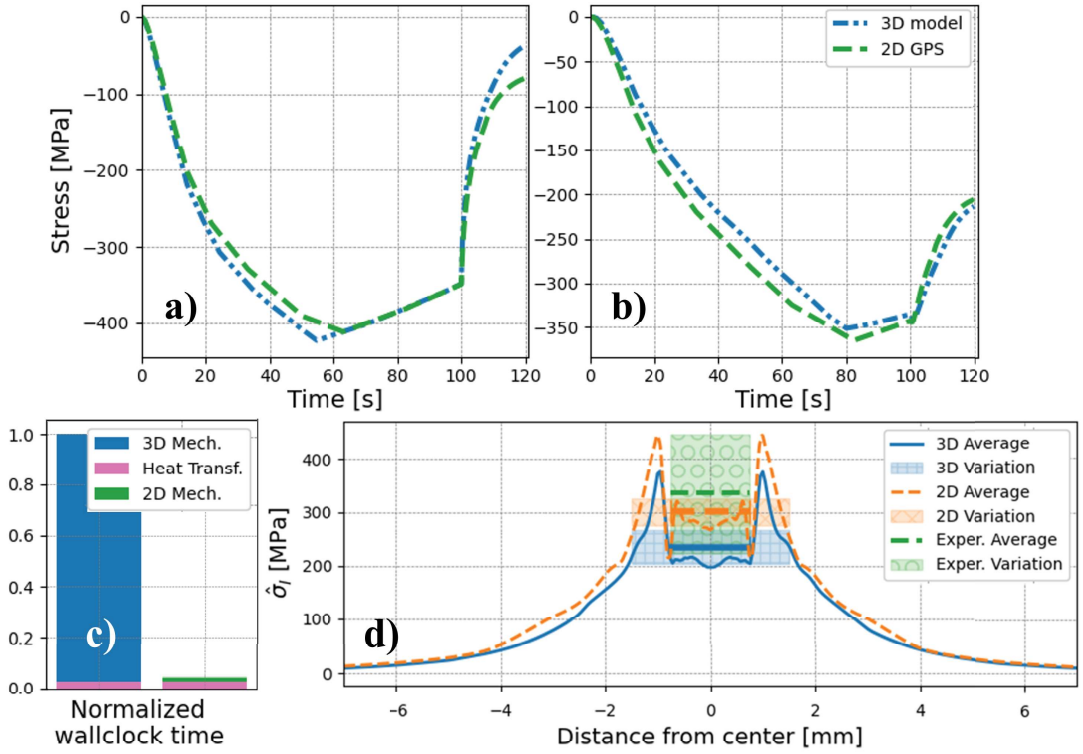

Figure 4.9: *Comparison of 3D and 2D GPS simulation results. (a) and (b) presents transient longitudinal stresses during preheating and one weld pass using the 3D and the 2D GPS model (from **Paper C**). (c) illustrates the computational times (from **Paper D**). (d) shows surface residual stresses following laser heating of an ER7T material sample obtained using the 3D and the 2D GPS models as well as experimental results (from **Paper D**).*

5 Rail repair welding simulations

5.1 Welding of rails

Rail welding serves two main purposes: joining rails during track construction and repairing damaged rail. In Sweden, rail sections are typically assembled by flash butt welding in a stationary plant before being transported to the field and joined by aluminothermic (thermite) welding [19]. In field repair welding, the damaged railhead material is removed and new material is added, layer by layer, using arc welding. All three welding processes induce phase transformations, residual stresses and variations in hardness and toughness, see e.g. [159, 160]. This makes continuously welded rails discontinuous in terms of microstructure, mechanical properties and residual stresses [161].

It is worth noting that these distinct rail welding processes differ significantly from conventional arc welding. Thermite welding closely resembles a casting process, whereas flash butt welding effectively forges the two rail ends together. Repair welding, as investigated in **Papers C** and **E**, differs from conventional arc welding in terms of material composition and welding process characteristics. The rail material has a higher carbon content than typical steels designed for welding, and the repair welding process is more akin to wire arc additive manufacturing (WAAM). Comparing the three rail welding processes, the lower heat input in repair welding affects a smaller area, resulting in higher cooling rates, and each new pass reheats the previous layers, causing more pronounced cyclic strain and an increased risk of martensite formation. This increased risk of unfavourable material phases is one of the motivations for the work presented in this thesis.

5.2 Repair welding simulation methodology

The simulation of repair welding places higher demands on numerical tools than thermite or flash butt welding due to the cyclic thermal loading and the complex evolution of the stress field and microstructure. As discussed in Section 4.3.3, numerical simulations with the required level of detail are computationally expensive. In response, **Paper C** presents a repair welding simulation methodology that combines the constitutive modelling from Chapter 3 together with the filler material and heat source modelling from Chapter 4 in a 2D Generalised Plane Strain (GPS) model of the rail cross-section. The 2D GPS models used for the mechanical part of the repair welding simulations presented in **Papers C** and **E** are shown in Figure 5.1. The figure illustrates how the 2D section is assumed to lie between two bounding rigid planes that are capable of axial translation (Δz) and rotation about the pitch and yaw axes about a defined pivot point ($\Delta\alpha$). These translation and rotation degrees of freedom allow the 2D model to simulate out-of-plane, membrane and bending behaviour.

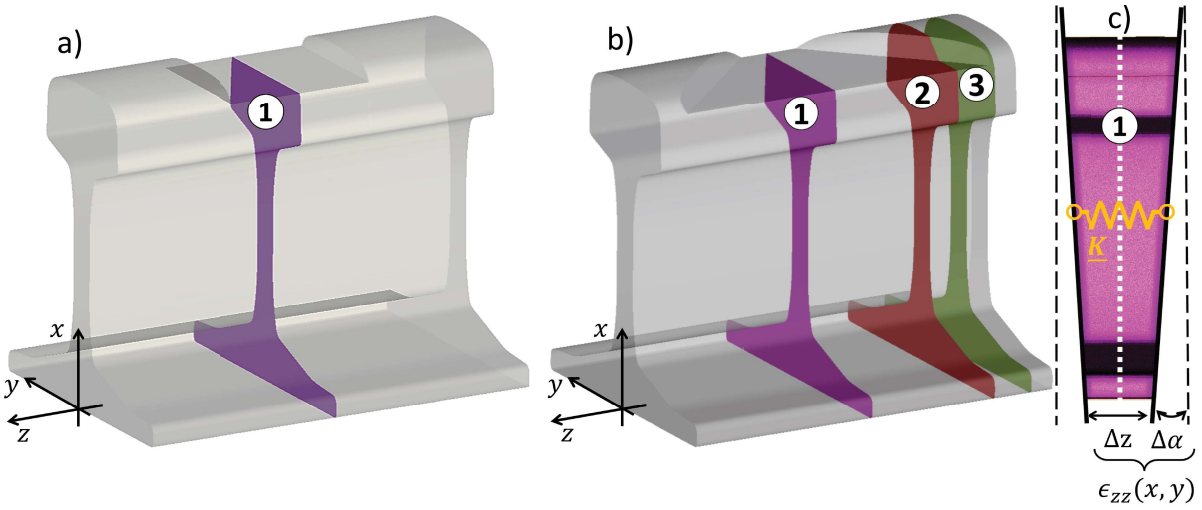

Figure 5.1: *Illustrations of railhead repair welding simulation models. a) the 3D and 2D model from* ***Paper C****. b) the 3D and three 2D models from* ***Paper E****. c) a schematic illustration of the 2D GPS model (from* ***Papers C*** *and* ***E****).*

When compared to the corresponding full-scale 3D simulation, as shown in Figure 4.9, the 2D GPS model reproduces the transient longitudinal stress component remarkably well at a fraction of the computational cost. This correlation is achieved by assigning axial and rotational stiffnesses to the degrees of freedom of the 2D model's bounding planes and matching these stiffnesses to those of the full-scale 3D FE model, schematically illustrated by the spring stiffness $\underline{\boldsymbol{K}}$ in Figure 5.1c. The numerical values of these stiffnesses have also been confirmed using Euler-Bernoulli beam theory. The methodology is further validated in **Papers C** and **D** by generating residual stresses that correlate well experimental stress measurements. As mentioned in Section 4.3.3, 2D welding simulation models have successfully reproduced the results of a 3D model several times in the past, typically for butt or fillet welds in plates. The 2D GPS model extends the ability of 2D models to be applied also to railhead repair welding.

Furthermore, in **Paper D**, simulations using the presented methodology provide detailed insights into the interaction between thermal strain and martensite transformation in both melted and non-melted material. The simulations illustrates how thermal contraction of previously melted material partially counteracts martensite expansion, leading to increased tensile stresses in the previously melted part of the martensite region. Experimental measurements confirm this phenomenon, validating not only the simulation methodology but also the constitutive material modelling, see Section 3.2. However, it should be noted, that the simulations presented in **Paper D** are for overlapping laser heating sequences rather than welding, i.e. no filler material is added.

5.3 Repair welding simulations

Although numerical simulations of railhead repair welding procedures are rare in the literature, notable examples are [128, 162, 148]. Compared to these examples, the material model used in **Papers C** and **E** allows for several interacting phenomena in CWM to be modelled in greater detail, e.g. homogenisation of multi-phase material states and virgin material state recovery. Furthermore, the presented simulation methodology uses other FEM-based simplifications, which allow for e.g. continuous addition of filler material and relatively fine FEM mesh discretization.

In **Paper C**, a repair welding experiment presented in [127, 128] is simulated and results are compared to the experimental measurements therein. This repair welding procedure consists of a rectangular cut-out of the railhead, see Figure 5.1a, followed by several longitudinal weld passes to fill this gap, illustrated in Figure 5.2a. In contrast, the repair welding procedure simulated in **Paper E** follows the Swedish regulations for stick welding railhead repairs [163, 164, 165]. Here, the cut-out is made with chamfers at 45°, see Figure 5.1b, and the repair weld is made by longitudinal passes along the outer edges of the rail followed by powerful zig-zag passes in between as is illustrated in Figure 5.2b. Comparing the two rail repair welding procedures, much fewer weld passes are simulated in **Paper C** than in **Paper E**, 12 and 86 passes respectively.

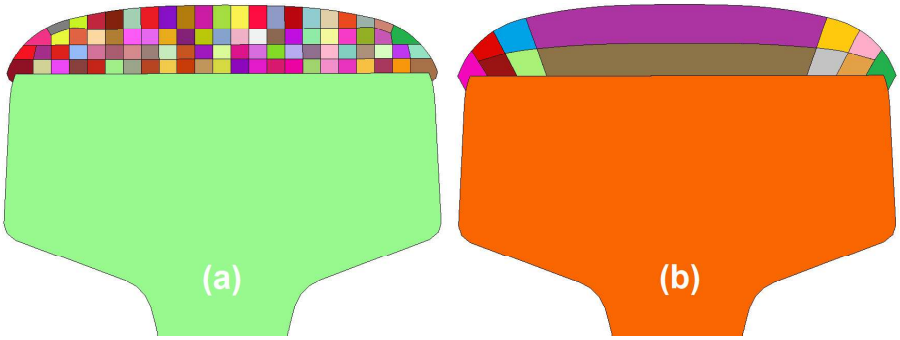

Figure 5.2: *Railhead repair welding 2D GPS simulation models for cross sections 1 of Figure 5.1a, from (a)* ***Paper C*** *and (b)* ***Paper E****. Separate colours indicate the individual weld passes.*

Figure 5.3 presents results from the repair welding experiment simulation presented in **Paper C**. The left graph compares the longitudinal residual stress to experimental measurements. Plotted from top to bottom through the centre of the 2D cross-section, the figure shows how simulation results correlate well with the experimental measurements, except for the surface measurement point. However, it is important to note that the experimental procedure included corrective grinding after the welding, which may induce compressive surface stresses, see e.g. [166]. The simulations do not explicitly include the grinding process, which could explain the discrepancy in the residual stresses on the rail surface. Furthermore, accident reports regarding the failure of repair welded rails

often indicate that the fusion zone between the filler and base material, as depicted in Figure 5.3b, is the critical region for fatigue crack initiation, rather than the surface [167]. This critical region is also supported by the findings of the over-rolling simulations performed in **Paper E** and presented in Section 5.4. The simulations demonstrate that operational loads result in a redistribution of residual stresses on the rail surface, while subsurface residual stresses remain high.

Furthermore, the study presented in **Paper C** also compares different homogenisation methods, as shown in Figure 5.3. These methods produce stress-time histories that differ significantly, resulting in distinct residual stresses due to the prolonged multi-phase material states caused by the transformation kinetics of the weld filler material. This significant difference in residual longitudinal stress is illustrated in Figures 5.3c and 5.3d. The self-consistent method provides the best overall correlation with experimental results and, as discussed in Section 3.3, gives a more physically correct material behaviour. Therefore, only the self-consistent homogenisation method was used in **Papers D** and **E**.

In **Paper E**, a rail repair welding process parameters study is presented. The study follows the Swedish repair welding regulations [163, 164, 165] and analyses how variations in preheat and operating temperature conditions, as well as variations in repair geometry affect the quality of the repaired rail. Simulation results for the reference case of the parameter study are presented in Figure 5.4, illustrating the material phases and longitudinal residual stress field for the three cross-sections presented in Figure 5.1b. Noteworthy findings of the process parameter study include that the powerful final zig-zag weld passes, illustrated in Figure 5.2b, generate significantly more heat than any additional pre-heating, re-heating or post-heating. The process is thereby quite robust in terms of its insensitivity to variations in the additional heating procedures. Moreover, in terms of unfavourable material phases and longitudinal tensile residual stresses, the most critical regions are identified at the final stretches of the repaired rail section where cooling rates are more rapid. This can be concluded from the material phases and tensile residual stresses presented in Figures 5.4b and 5.4e illustrating the rail cross-sections at the final stretch of the repair (highlighted in Figure 5.1b).

When comparing the two welding procedures discussed in **Papers C** and **E**, it should be noted that the process parameter study in **Paper E** also examines a rectangular railhead cutout similar to that used in **Paper C** (see Figures 5.1a and 5.1b). The parameter study shows that the rectangular railhead cutout results in higher residual tensile stresses compared to the chamfered railhead cutout used in the Swedish regulatory procedure. This difference can be observed by comparing the results shown in Figures 5.3d and 5.4d. Furthermore, the zig-zag weld passes in Swedish procedure prove to be advantageous in maintaining the operating temperature above the martensite starting temperature for a longer duration and over a larger region compared to the longitudinal weld passes used in **Paper C**. This can be concluded by comparing the results presented in Figures 5.3b and 5.4a. These results indicate that the welding directions used when adding new rail material, i.e. the build-up paths, significantly affects quality of the repaired rail. This is

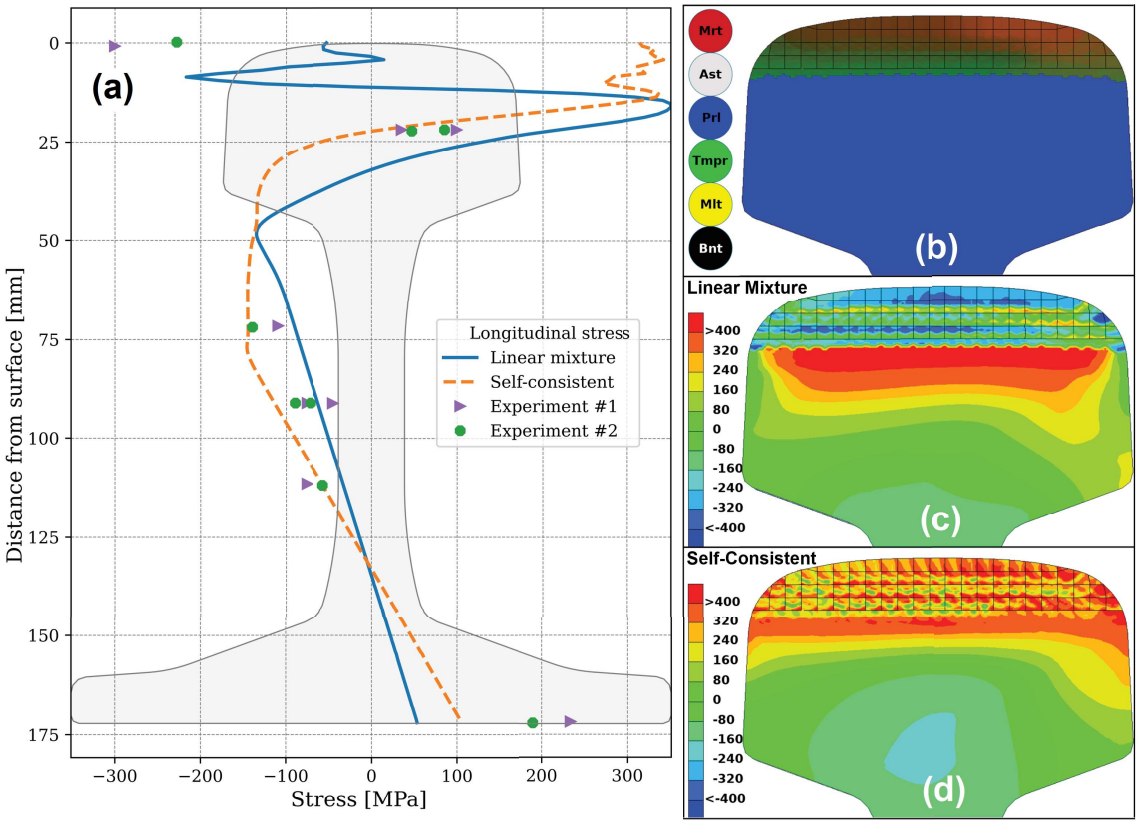

Figure 5.3: *Railhead repair welding simulation results from* ***Paper C****, illustrating the cross-section presented in Figure 5.1a. (a) Longitudinal residual stress along the center-line of the repaired cross section, simulation results obtained using the linear mixture and self-consistent homogenisation methods, experimental results obtained from [128]. (b) Material phases resulting from the repair welding. (c) and (d) Longitudinal residual stress field obtained using the linear mixture and self-consistent method, respectively.*

anticipated when considering the aforementioned similarity to WAAM, where the effects of different build-up path strategies have been investigated both experimentally and numerically, see e.g. [168] and [169].

Furthermore, as discussed in Section 5.1, the different rail welding processes are inherently different and results in dissimilar residual stress fields. Flash butt and thermite welding involve high heat input over the entire rail cross section, leading to slow and uniform cooling. Whereas repair welding, as presented in **Papers C** and **E**, involves lower and cyclic local heat input in the railhead, resulting in faster cooling and more complex microstructure evolution. Consequently, the temperature gradients during these welding procedures are significantly different, resulting in distinct residual stress states. Flash-butt and thermite welding typically result in a compressive longitudinal residual stress field in the rail toe and head, and a tensile stress field in the rail web, see e.g. [19, 170]. In contrast, railhead repair welding produces the opposite relationship between

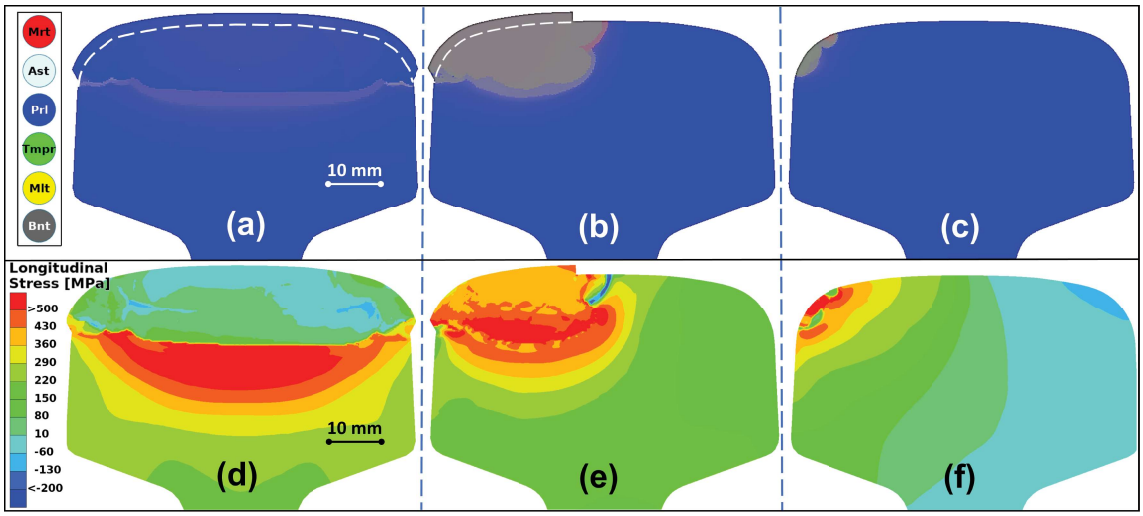

Figure 5.4: *Railhead repair welding simulation results from* ***Paper D****, illustrating the three cross-sections presented in Figure 5.1b. (a), (b) and (c) material phases resulting from the repair welding for cross-sections 1, 2 and 3, respectively. (d), (e) and (f) longitudinal residual stress field obtained using the self-consistent method for cross-sections 1, 2 and 3, respectively.*

tensile and compressive stresses, as illustrated in Figure 5.3a. Hence, the residual stresses resulting from repair welding may be more critical in terms of initiating fatigue cracks. This is one of the motivating factors behind the studies presented in **Papers C** and **E**.

5.4 Railhead repair performance

There is a general consensus in the research community that rail welds constitute a weak point in the railway network. It is estimated that between 25% and 70% of rail failures occur in the vicinity of welds, depending on the type of rail and traffic, see e.g. [171, 172, 173]. Residual stresses resulting from flash butt welding, thermite welding and railhead repair welding differ from manufacturing residual stresses and can adversely affect rail performance, see e.g. [174, 175]. Rail welding also introduces additional complexities not considered in the appended papers, such as surface irregularities that increase dynamic loads, see e.g. [176, 177], subsurface defects that degrade fatigue properties, see e.g. [178], and a microstructure with varying grain size, see e.g. [179]. The quality of a rail weld is therefore not only determined by its residual condition, but also by its mechanical performance under operational service loading. Therefore, rail welding simulations often include over-rolling simulations to evaluate the fatigue performance of welded rail sections, see e.g. [180, 181, 182, 183]. For this reason, in **Paper E**, the repair welding simulation methodology is extended to also include over-rolling simulations and evaluation of fatigue crack initiation.

The over-rolling simulation setup uses parts of the over-rolling simulation procedure presented in [184]. Starting from field measurements, a 2D equivalent over-rolling load sequence is derived from 3D Hertzian contact loads. In short, the equivalent loads implemented in the 2D GPS model use scaling of the boundary load per unit length to match the same maximum von Mises stress as from a metamodel of 3D elasto-plastic normal contact. The metamodel accounts for local radii at the wheel-rail contact points, cf. [185]. The factors used in the scaling are computed a priori and implemented through the force equilibrium in the element assembly of the FE-solver. Only normal and lateral contact loads are considered in the simulations. However, the degrees of freedom of the cross-section bounding planes of the 2D GPS model allow for bending and axial loads in the rail to be included. The contact loads are obtained from multi-body dynamic simulations performed in [186], where a curved rail section along the western mainline in Sweden was simulated. In these multi-body simulations, a typical traffic sequence for the curve was used with representative variations of vehicle type (90% passenger trains and , axle loads from 11.7 to 21.0 tonnes), wheel profile (based on 279 measured profiles) and vehicle speed. The defined representative traffic sequence contained 483 different wheel passages. The sequence is repeated several times to generate 2000 of over-rolling wheel passages.

Figure 5.5 shows the longitudinal residual stresses resulting from the simulated over-rolling simulations in **Paper E**. A comparison of these results with the welding residual stresses presented in Figure 5.4 reveals that the welding residual stresses on the rail surface tend to be redistributed and alleviated by train wheel passages. However, welding residual stresses at some distance below the rail surface exceed over-rolling stresses by an order of magnitude. As a result, the over-rollings have less impact on the stress state in this region. Similar trends of surface residual stress redistribution are also observed in simulations of flash butt and thermite welding over-rollings, see e.g. [170, 187].

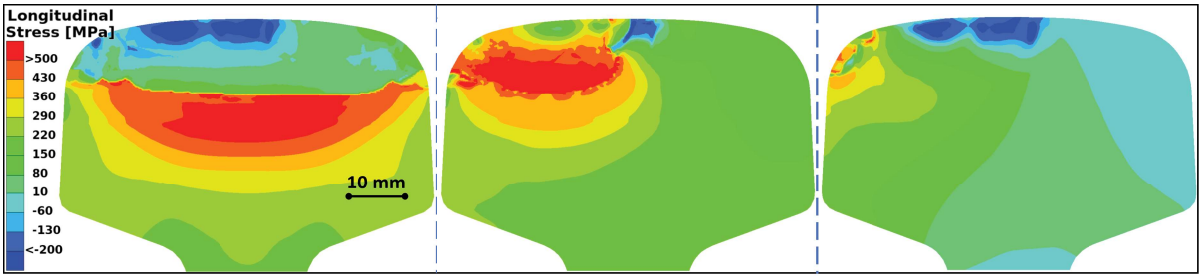

Figure 5.5: *Over-rolling simulation results from* ***Paper D****, illustrating how the repair welding residual stresses presented in Figure 5.4 are affected by post-repair operational loads. (a), (b) and (c) presents longitudinal residual stress field obtained using the self-consistent method for cross-sections 1, 2 and 3, respectively.*

In **Paper E**, the impact of repair weld residual stresses during operational over-rolling loading is evaluated using the Dang Van stress fatigue criterion. This criterion is often used in fatigue analysis for railway applications, see e.g. [188, 189, 162]. When interpreting the Dang Van stresses calculated in **Paper E**, it is important to consider the limitations of the 2D GPS model and the simplified modelling of the over-rollings. With these limitations, the evaluation should be restricted to qualitative comparisons of the fatigue performance effects of varying repair welding process parameters. In this context, most of the repair welding cases considered in the parameter study produce similar Dang Van stress results. Comparison with over-rolling simulation results from an unrepaired rail demonstrates that fatigue performance improves in regions of high compressive residual stress and worsens in regions of tensile residual stress, as expected.

It should be noted that, similar to welding simulations, full-scale 3D wheel-rail rolling contact simulations require significant computational resources. Simulating a single day's traffic can take weeks [190]. Even with advanced simulation techniques, achieving a computation time of less than one minute per over-rolling cycle is challenging [191]. Consequently, over-rolling simulations often use 2D models in the length direction of the rail, see e.g. [192, 193], rather than the transverse rail cross-sectional models used for the repair welding simulations presented in **Papers C** and **E**. As a rough comparison of computational time, the over-rolling method implemented in **Paper E** performs about three over-rollings per minute of calculation time.

When comparing the over-rolling simulations presented in **Papers A** and **E**, an apparent difference is that the former focuses on the wheel, whereas the latter focuses on the rail. However, there are several similarities between the studies. The 3D simulations in **Paper A** also use a discretisation of the transient rolling contact problem by simulating a traversing contact pressure distribution on the wheel tread. The shape of the pressure distribution is estimated using a super-ellipsoid, which is adjusted to match indentation simulations as presented in [17]. This approximation takes into account both the stiffness variation due to the wheel flat and the traction variation in the contact patch. Although the load magnitudes in **Papers A** and **E** are comparable (20 tonne axle load), the traction loads are different. **Paper A** uses a tangential traction load simulating a brake or drive wheel, while the 2D simulation in **Paper E** uses a transverse traction load derived from multi-body simulations of a curved track section. Comparing the simulation results, both studies show that during over-rolling, residual stresses induced by thermal loads are redistributed at the surface, but increased a short distance below the surface. Highlighting the subsurface region as the most critical in terms of the risk of fatigue crack initiation due to unfavourable material phases and residual stresses following thermal loading.

6 Concluding Remarks and Future Work

6.1 Concluding Remarks

A phenomenological material model was developed for thermo-mechanically loaded pearlitic steels, incorporating cyclic plasticity, phase transformation kinetics and analytically based multi-phase homogenisation. The phase transformations considered included austenitisation, tempering of martensite and bainite during heating and transformation of austenite to pearlite, bainite or martensite during cooling. Cyclic plasticity was modelled using a Chaboche plasticity model with a von Mises yield function, non-linear isotropic and kinematic hardening, temperature dependent material parameters and transformation-induced plasticity.

Dilatation simulations using the developed constitutive material model showed that the choice of homogenisation method played a crucial role in the resulting stress-strain state. This was particularly evident during multi-phase stages and cyclic thermal loading. Four homogenisation methods were compared: isostrain, isostress, a linear mixture rule, and a self-consistent method. Of the four, the self-consistent method was shown to produce the most physically accurate material behaviour. The numerical demonstrations also highlighted the importance of the model's ability to account for the recovery of a virgin material state during cyclic melting and solidification.

The material model has been implemented in finite element simulations of a double wheel flat, involving two heat pulses on the tread of a railway wheel, followed by about ten over-rollings. The simulations used a one-way coupling between the thermal and the mechanical fields, where the temperature field from the heat transfer analysis drives the subsequent mechanical analysis. The two heat pulses induced subsurface residual tensile stresses which slightly redistributed and, importantly, stabilised during the over-rollings.

A railhead repair welding simulation methodology was developed incorporating the material model. This methodology takes advantage of the axially uniform rail geometry and combines a 3D heat transfer simulation with a 2D mechanical simulation. The 2D model is a generalised plane strain model of the rail cross-section, which takes the out-of-plane axial and bending stiffnesses of the rail into account. This methodology reduces the immense computational cost normally associated with full-scale multi-pass welding simulations, while still incorporating several interacting thermo-metallurgical-mechanical phenomena of the welding process. The methodology was able to replicate the results of the more computationally intensive 3D model and demonstrated reasonable agreement with residual stress measurements from literature. Additionally, a laser heating experiment was carried out further tune and validate the methodology. The simulations were able to replicate residual stresses and material phases, as well as providing valuable insights into the interaction between thermal strain and martensite transformation in both melted and non-melted material.

The simulation methodology was used in a railhead repair welding process parameter study to investigate the effect of variations in preheating, operating temperatures and repair geometry on the residual stress state and the resulting material phases. Additionally, a railhead welding experiment was conducted to tune the heat source modelling of the welding simulations. The parameter study revealed that the powerful final weld passes contribute significantly to the robustness of the process, making it less sensitive to variations in additional heating procedures. Consistent with field observations, the simulations identified the fusion zone of the base and filler materials, at the start and end stretches of the repaired rail section, as the critical regions in terms of unfavourable material phases and residual stresses.

Furthermore, the simulation methodology was extended to include over-rolling simulations, which represent train wheel passages on the repaired rail surface. The risk of mechanical fatigue crack initiation was evaluated by comparing the Dang Van stress of the repaired rail to that of an un-repaired rail, based on the results of 2000 simulated wheel passages. The study demonstrated that welding residual tensile stresses at the rail surface are redistributed and relieved by over-rollings, while residual stresses some distance below the rail surface are less affected and remain high.

In summary, the research in this thesis achieved several key objectives outlined at the outset. Firstly, a material model was further developed to accurately simulate the thermo-metallurgical-mechanical behaviour of pearlitic steels under cyclic high-temperature processes. Secondly, the model was integrated into a computationally efficient finite element framework, allowing simulations of various railway scenarios, including railhead repair welding processes, heating events on the train wheel thread, and over-rolling simulations. Furthermore, several results were validated against experimental data to ensure simulation accuracy. Although significant progress was made towards achieving the stated objectives, there are still areas for potential future research, which are outlined in the following section.

6.2 Outlook

Whilst the presented results underline the efficiency and accuracy of the material modelling and finite element simulation methodology, it is important to note that several simplifications and assumptions have been introduced which warrant further investigation of their impact. Some possible directions for future work are outlined below, divided into the categories of improving material modelling techniques and developing finite element method process simulations.

- **Material modelling**

  The effects of including viscous material behaviour at higher temperatures and physically based annealing in the modelling can be substantial during the prolonged stages at elevated temperatures occurring in repair welding. The impact of including these effects in the welding simulation methodology could be investigated.

  Internal variable inheritance can be examined for better understanding and more realistic modelling of how history effects of hardening and plasticity are transferred from the parent phase to the nucleating phase. The development of a material phase inheritance rule would be required.

  The heat transfer simulation could be extended to account for latent heat during phase transformations. Its influence might be considerable when cooling rates are relatively slow, e.g. in certain repair welding procedures.

  To increase the reliability of the simulation results, it is necessary to improve the database of phase-specific material properties and calibrate the models accordingly. For instance, the material parameters related to transformation induced plasticity can be further investigated.

  Repair welding simulations show that both martensite and bainite transformations are likely to occur, and tempering of these transformations is expected. Improvements in modelling of the tempering process could enhance the simulation outcomes.

  Based on their effect on simulation outcomes, further investigation into homogenisation methods may be worthwhile, e.g. using the iso-work method or multi-scale modelling techniques. Also, multi-stage homogenisation may be explored to simulate a parent and nucleating phase transforming while surrounded by a non-participating matrix phase.

- **Finite element simulations**

  The fidelity of the simulation procedure could be improved by more advanced tuning of the heat source modelling, preferably using transient temperature history measurements.

  Simulation results from the presented methodology can be compared to those obtained from commercial welding simulation softwares. Additionally, it may be worthwhile to investigate the use of commercial software to facilitate the FE-model setup procedure for large-scale simulations.

  The ability to use the presented methodology to simulate other important railway maintenance actions such as corrective grinding of the rail can be investigated.

  The over-rolling simulations could be developed further by considering additional realistic conditions and contact loading scenarios. For instance, including axial and bending loads in the rail may improve the understanding of rail fatigue performance.

Studying the influence of in-service operational parameters, such as train speed and axle loads, on the repaired rail performance can provide valuable insights for process optimisation. Similarly, the effect of post-repair subsurface material heterogeneities and defects could also be studied.

Although the 2D simulation procedure is limited to axially uniform geometries, it may be useful in other manufacturing processes, such as wire arc additive manufacturing, and for materials other than pearlitic steels. Additionally, it may be worth exploring the possibility of using multiple 2D simulations to obtain an interpolated representation of the material state in a 3D structure.

This outlook sets the stage for future research initiatives, aligning with the continuous pursuit of advancements in the field of rail welding and thermo-metallurgical-mechanical simulations.

References

[1] J. P. Rodrigue, C. Comtois, and B. Slack. *The geography of transport systems*. Vol. Fourth edition. Routledge, 2016.

[2] U. N. G. Assembly. *Transforming our world: the 2030 Agenda for Sustainable Development*. A/RES/70/1. 2015.

[3] C. Doll, C. Brauer, J. Köhler, and P. Scholten. *Methodology for GHG Efficiency of Transport Modes*. Karlsruhe, Germany: Fraunhofer-Institute for Systems and Innovation Research ISI, 2020.

[4] *White paper: Roadmap to a Single European Transport Area – Towards a competitive and resource efficient transport system*. Brussels: European Commision (EC), 2011.

[5] *Commission Communication: A Roadmap for moving to a competitive low carbon economy in 2050*. Brussels: European Commision (EC), 2011.

[6] U. N. G. Assembly. *The Sustainable Development Goals Report 2023: Special edition*. 2023.

[7] M. A. Arslan and O. Kayabaşı. 3-D Rail–Wheel contact analysis using FEA. *Advances in Engineering Software* 45.1 (2012), 325–331.

[8] A. Kapoor, F. Franklin, S. Wong, and M. Ishida. Surface roughness and plastic flow in rail wheel contact. *Wear* 253.1 (2002). CM2000 S.I., 257–264.

[9] H. Brunskill, A. Hunter, L. Zhou, R. D. Joyce, and R. Lewis. An evaluation of ultrasonic arrays for the static and dynamic measurement of wheel–rail contact pressure and area. *Proceedings of the Institution of Mechanical Engineers, Part J: Journal of Engineering Tribology* 234.10 (2020), 1580–1593.

[10] A. Ekberg. "Fatigue of railway wheels". *Wheel–Rail Interface Handbook*. Ed. by R. Lewis and U. Olofsson. Woodhead Publishing, 2009, pp. 211–244.

[11] S. M. Famurewa, A. Nissen, and U. Kumar. "Scheduling of Railway Infrastructure Maintenance Tasks Using Train Free Windows". *Current Trends in Reliability, Availability, Maintainability and Safety*. Cham: Springer International Publishing, 2016, pp. 425–436.

[12] L. Ferreira and M. H. Murray. Modelling rail track deterioration and maintenance: current practices and future needs. *Transport Reviews* 17.3 (1997), 207–221.

[13] C. Jessop, J. Ahlström, C. Persson, and Y. Zhang. Damage evolution around white etching layer during uniaxial loading. *Fatigue & Fracture of Engineering Materials & Structures* 43.1 (2020), 201–208.

[14] S. Niederhauser, B. Karlsson, and P. Sotkovszki. Microstructural development in the heat-affected zone of a laser-cladded steel. *International Journal of Materials Research* 96.4 (2005), 370–376.

[15] J. Ahlström and B. Karlsson. Analytical 1D model for analysis of the thermally affected zone formed during railway wheel skid. *Wear* 232.1 (1999), 15–24.

[16] K. Cvetkovski and J. Ahlström. Characterisation of plastic deformation and thermal softening of the surface layer of railway passenger wheel treads. *Wear* 300.1 (2013), 200–204.

[17] A. Esmaeili, M. S. Walia, K. Handa, K. Ikeuchi, M. Ekh, T. Vernersson, and J. Ahlström. A methodology to predict thermomechanical cracking of railway wheel treads: From experiments to numerical predictions. *International Journal of Fatigue* 105.Supplement C (2017), 71–85.

[18] J. Jergéus. Martensite formation and residual stresses around railway wheel flats. *Proceedings of the Institution of Mechanical Engineers, Part C: Journal of Mechanical Engineering Science* 212.1 (1998), 69–79.

[19] A. Skyttebol and B. L. Josefson. "Numerical simulation of flash butt welding of railway rails". *Mathematical modelling of weld phenomena 7*. Ed. by H. Cerjak, H. K. D. H. Bhadeshia, and E. Kozeschnik. Graz, Austria: Verlag der Technischen Universität Graz, 2004, pp. 943–964.

[20] J. Ahlström and B. Karlsson. Modelling of heat conduction and phase transformations during sliding of railway wheels. *Wear* 253.1 (2002), 291–300.

[21] S. Caprioli and A. Ekberg. Numerical evaluation of the material response of a railway wheel under thermomechanical braking conditions. *Wear* 314.1 (2014). Proceedings of the 9th International Conference on Contact Mechanics and Wear of Rail / Wheel Systems, Chengdu, 2012, 181–188.

[22] H. Bhadeshia and R. Honeycombe. *Steels: microstructure and properties*. Vol. Fourth edition. Oxford: Butterworth-Heinemann, 2017.

[23] E. Pereloma and D. Edmonds. *Phase Transformations in Steels. Volume 1: Fundamentals and Diffusion-Controlled Transformations*. Cambridge: Woodhead Publishing Limited, 2012.

[24] D. Nikas. "Influence of combined thermal and mechanical loadings on pearlitic steel microstructure in railway wheels and rails". PhD thesis. Chalmers University of Technology, 2018.

[25] *Railway applications - Wheelsets and bogies - Wheels - Product requirement. EN 13262:2004+A1*. Brussels: European Committee for Standardization (CEN), 2004.

[26] *Railway applications. Track. Rail. Vignole railway rails 46 kg/m and above, BS EN 13674-1:2011+A1:2017*. Brussels: European Committee for Standardization (CEN), 2011.

[27] H. Bhadeshia and R. Honeycombe. *Steels: Microstructure and Properties*. Oxford, UK: Butterworth-Heinemann, 2017.

[28] H. Bhadeshia. *Theory of Transformations in Steels*. 1st ed. Boca Raton, Florida, USA: CRC Press, 2021.

[29] H. Bhadeshia. *Bainite in Steels: Theory and Practice*. 3rd ed. London, UK: CRC Press, 2015.

[30] Sente-Software. *JMatPro 6.0*. Version 6.0. May 25, 2018.

[31] S. Sjöström. Interactions and constitutive models for calculating quench stresses in steel. *Materials Science and Technology* 1 (1985), 823–829.

[32] S. Denis, S. Sjöstrom, and A. Simon. Coupled Temperature, Stress, Phase Transformation Calculation Model Numerical Illustration of the Internal Stresses Evolution during Cooling of a Eutectoid Carbon Steel Cylinder. *Metallurgical Transactions A* 18.July (1987), 1203–1212.

[33] R. Mahnken, A. Schneidt, and T. Antretter. Macro modelling and homogenization for transformation induced plasticity of a low-alloy steel. *International Journal of Plasticity* 25.2 (2009), 183–204.

[34] T. Inoue and B. Raniecki. Determination of thermal-hardening stress in steels by use of thermoplasticity theory. *Journal of the Mechanics and Physics of Solids* 26.3 (1978), 187–212.

[35] M. Wolff, M. Böhm, and D. Helm. Material behavior of steel – Modeling of complex phenomena and thermodynamic consistency. *International Journal of Plasticity* 24.5 (2008), 746–774.

[36] M. Ghafouri, J. Ahn, J. Mourujärvi, T. Björk, and J. Larkiola. Finite element simulation of welding distortions in ultra-high strength steel S960 MC including comprehensive thermal and solid-state phase transformation models. *Engineering Structures* 219 (2020), 110804.

[37] F. Fischer, G. Reisner, E. Werner, K. Tanaka, G. Cailletaud, and T. Antretter. A new view on transformation induced plasticity (TRIP). *International Journal of Plasticity* 16.7 (2000), 723–748.

[38] H. Hallberg, P. Håkansson, and M. Ristinmaa. A constitutive model for the formation of martensite in austenitic steels under large strain plasticity. *International Journal of Plasticity* 23.7 (2007), 1213–1239.

[39] T. Iwamoto and T. Tsuta. Computational simulation on deformation behavior of CT specimens of TRIP steel under mode I loading for evaluation of fracture toughness. *International Journal of Plasticity* 18.11 (2002), 1583–1606.

[40] M. Militzer, M. Mecozzi, J. Sietsma, and S. van der Zwaag. Three-dimensional phase field modelling of the austenite-to-ferrite transformation. *Acta Materialia* 54.15 (2006), 3961–3972.

[41] V. Kouznetsova and M. Geers. A multi-scale model of martensitic transformation plasticity. *Mechanics of Materials* 40.8 (2008), 641–657.

[42] S. Denis, D. Farias, and A. Simon. Mathematical Model Coupling Phase Transformations and Temperature Evolutions in Steels. *ISIJ International* 32.3 (1992), 316–325.

[43] F. M. B. Fernandes, S. Denis, and A. Simon. Mathematical model coupling phase transformation and temperature evolution during quenching of steels. *Materials Science and Technology* 1.10 (1985), 838–844.

[44] E. Scheil. Anlaufzeit der austenitumwandlung. *Archiv für das Eisenhüttenwesen* 8.12 (1935), 565–567.

[45] C. Verdi and A. Visintin. A mathematical model of the austenite-pearlite transformation in plain carbon steel based on the Scheil's additivity rule. *Acta Metallurgica* 35.11 (1987), 2711–2717.

[46] B. Singh, P. Singhal, K. K. Saxena, and R. K. Saxena. Influences of Latent Heat on Temperature Field, Weld Bead Dimensions and Melting Efficiency During Welding Simulation. *Metals and Materials International* 27.8 (2021), 2848–2866.

[47] Z. Li, G. Yu, X. He, S. Li, C. Tian, and B. Dong. Analysis of surface tension driven flow and solidification behavior in laser linear welding of stainless steel. *Optics and Laser Technology* 123 (2020), 105914.

[48] G. G. Roy, J. W. Elmer, and T. DebRoy. Mathematical modeling of heat transfer, fluid flow, and solidification during linear welding with a pulsed laser beam. *Journal of Applied Physics* 100.3 (2006).

[49] D. Koistinen and R. Marburger. A general equation prescribing the extent of the austenite-martensite transformation in pure iron-carbon alloys and plain carbon steels. *Acta Metallurgica* 7.1 (1959), 59–60.

[50] K. Cvetkovski, J. Ahlström, and B. Karlsson. Influence of short heat pulses on properties of martensite in medium carbon steels. *Materials Science and Engineering: A* 561 (2013), 321–328.

[51] M. Wolff, M. Böhm, G. Löwisch, and A. Schmidt. Modelling and testing of transformation-induced plasticity and stress-dependent phase transformations in steel via simple experiments. *Computational Materials Science* 32.3 (2005). IWCMM, 604–610.

[52] S. Denis. Considering stress-phase transformation interactions in the calculation of heat treatment residual stresses. *Le Journal de Physique IV* 6.C1 (1996), 159–174.

[53] H. Hallberg, P. Håkansson, and M. Ristinmaa. Thermo-mechanically coupled model of diffusionless phase transformation in austenitic steel. *International Journal of Solids and Structures* 47.11 (2010), 1580–1591.

[54] B. Starman, H. Hallberg, M. Wallin, M. Ristinmaa, and M. Halilovič. Differences in phase transformation in laser peened and shot peened 304 austenitic steel. *International Journal of Mechanical Sciences* 176 (2020), 105535.

[55] V. I. Levitas. Thermomechanical theory of martensitic phase transformations in inelastic materials. *International Journal of Solids and Structures* 35.9 (1998), 889–940.

[56] R. Mahnken, M. Wolff, A. Schneidt, and M. Böhm. Multi-phase transformations at large strains – Thermodynamic framework and simulation. *International Journal of Plasticity* 39 (2012), 1–26.

[57] M. Coret and A. Combescure. A mesomodel for the numerical simulation of the multiphasic behavior of materials under anisothermal loading (application to two low-carbon steels). *International Journal of Mechanical Sciences* 44.9 (2002), 1947–1963.

[58] N. Häberle, A. Pittner, R. Falkenberg, O. Kahlcke, and M. Rethmeier. Application of multi-phase viscoplastic material modelling to computational welding mechanics of grade-s960ql steel. *Comptes Rendus Mécanique* 346.11 (2018). Computational methods in welding and additive manufacturing Simulation numérique des procédés de soudage et fabrication additive, 1018–1032.

[59] J. Lemaitre and J. L. Chaboche. *Mechanics of solid materials*. 2nd. Cambridge, UK: Cambridge University Press, 1994.

[60] J. Chaboche. Constitutive equations for cyclic plasticity and cyclic viscoplasticity. *International Journal of Plasticity* 5.3 (1989), 247–302.

[61] C. O. Frederick and P. J. Armstrong. A mathematical representation of the multiaxial Bauschinger effect. *Materials at High Temperatures* 21.1 (2014), 1–26.

[62] S. Bari and T. Hassan. Anatomy of coupled constitutive models for ratcheting simulation. *International Journal of Plasticity* 16.3 (2000), 381–409.

[63] J. Chaboche. A review of some plasticity and viscoplasticity constitutive theories. *International Journal of Plasticity* 24.10 (2008), 1642–1693.

[64] D. Nikas, J. Ahlström, and A. Malakizadi. Mechanical properties and fatigue behaviour of railway wheel steels as influenced by mechanical and thermal loadings. *Wear* 366-367.Supplement C (2016), 407–415.

[65] J. Draxler, J. Edberg, J. Andersson, and L. E. Lindgren. Modeling and simulation of weld solidification cracking part III: Simulation of solidification cracking in Varestraint tests of alloy 718. *Welding in the World* 63.6 (2019), 1883–1901.

[66] S. D. Banik, S. Kumar, P. K. Singh, S. Bhattacharya, and M. M. Mahapatra. Distortion and residual stresses in thick plate weld joint of austenitic stainless steel: Experiments and analysis. *Journal of Materials Processing Technology* 289 (2021), 116944.

[67] E. D. Derakhshan, N. Yazdian, B. Craft, S. Smith, and R. Kovacevic. Numerical simulation and experimental validation of residual stress and welding distortion induced by laser-based welding processes of thin structural steel plates in butt joint configuration. *Optics and Laser Technology* 104 (2018), 170–182.

[68] C. Elcoate, R. Dennis, P. Bouchard, and M. Smith. Three dimensional multi-pass repair weld simulations. *International Journal of Pressure Vessels and Piping* 82.4 (2005). Residual Stresses at Repair Welds, 244–257.

[69] G. W. Greenwood and R. Johnson. The deformation of metals under small stresses during phase transformations. *Proceedings of the Royal Society of London. Series A. Mathematical and Physical Sciences* 283.1394 (1965), 403–422.

[70] C. L. Magee. "Transformation kinetics, microplasticity and aging of martensite in Fe-31Ni". PhD thesis. Carnegie Institute of Technology, Pittsburgh, Pa, 1966.

[71] M. Wolff, M. Böhm, and B. Suhr. Comparison of different approaches to transformation-induced plasticity in steel. *Materialwissenschaft und Werkstofftechnik: Entwicklung, Fertigung, Prüfung, Eigenschaften und Anwendungen technischer Werkstoffe* 40.5-6 (2009), 454–459.

[72] J. Leblond, G. Mottet, and J. Devaux. A theoretical and numerical approach to the plastic behaviour of steels during phase transformations—II. Study of classical plasticity for ideal-plastic phases. *Journal of the Mechanics and Physics of Solids* 34.4 (1986), 411–432.

[73] P. Dong. On repair weld residual stresses and significance to structural integrity. *Welding in the World* 62.2 (2018), 351–362.

[74] M. Chiumenti, M. Cervera, A. Salmi, C. Agelet de Saracibar, N. Dialami, and K. Matsui. Finite element modeling of multi-pass welding and shaped metal deposition processes. *Computer Methods in Applied Mechanics and Engineering* 199.37 (2010), 2343–2359.

[75] M. Fisk and A. Lundbäck. Simulation and validation of repair welding and heat treatment of an alloy 718 plate. *Finite Elements in Analysis and Design* 58 (2012), 66–73.

[76] J. Bergheau, Y. Vincent, J. Leblond, and J. Jullien. Viscoplastic behaviour of steels during welding. *Science and Technology of Welding and Joining* 9.4 (2004), 323–330.

[77] A. S. Oddy, J. A. Goldak, and J. M. McDill. Transformation plasticity and residual stresses in single-pass repair welds. *Journal of Pressure Vessel Technology, Transactions of the ASME* 114.1 (1992), 33–38.

[78] J. Ronda and G. Oliver. Consistent thermo-mechano-metallurgical model of welded steel with unified approach to derivation of phase evolution laws and transformation-induced plasticity. *Computer Methods in Applied Mechanics and Engineering* 189.2 (2000), 361–418.

[79] L. Depradeux and R. Coquard. Influence of viscoplasticity, hardening, and annealing effects during the welding of a three-pass slot weld (NET-TG4 round robin). *International Journal of Pressure Vessels and Piping* 164 (2018). NeT TG4 Weld Residual Stress Benchmark Simulation and Measurement Round Robins, 39–54.

[80] A. Maekawa, A. Kawahara, H. Serizawa, and H. Murakawa. Fast three-dimensional multipass welding simulation using an iterative substructure method. *Journal of Materials Processing Technology* 215 (2015), 30–41.

[81] L. Mouelle, F. Praud, G. Chatzigeorgiou, F. Meraghni, J. Serri, and E. Fleury. Thermally-activated hardening recovery of thermo-elasto-plastic metals during annealing: Constitutive modeling for the simulation of welding process. *Mechanics of Materials* 140 (2020), 103218.

[82] C. Şimşir and C. H. Gür. A FEM based framework for simulation of thermal treatments: Application to steel quenching. *Computational Materials Science* 44.2 (2008), 588–600.

[83] R. G. Stringfellow, D. M. Parks, and G. B. Olson. A constitutive model for transformation plasticity accompanying strain-induced martensitic transformations in metastable austenitic steels. *Acta Metallurgica Et Materialia* 40.7 (1992), 1703–1716.

[84] O. Bouaziz and P. Buessler. Iso-work increment assumption for heterogeneous material behavior modelling. *Advanced Engineering Materials* 6.1-2 (2004), 79–83.

[85] J. D. Eshelby. The determination of the elastic field of an ellipsoidal inclusion, and related problems. *Proceedings of the royal society of London. Series A. Mathematical and physical sciences* 241.1226 (1957), 376–396.

[86] J. Hutchinson. Elastic-plastic behaviour of polycrystalline metals and composites. *Proceedings of the Royal Society A: Mathematical, Physical and Engineering Sciences* 319 (1970), 247–272.

[87] R. A. Lebensohn, P. A. Turner, J. W. Signorelli, and G. R. Canova. Calculation of intergranular stresses based on a large-strain viscoplastic self-consistent polycrystal model. *Modelling and Simulation in Materials Science and Engineering* 6.April 1998 (1998), 447–465.

[88] L. E. Lindgren, A. Lundbäck, M. Fisk, R. Pederson, and J. Andersson. Simulation of additive manufacturing using coupled constitutive and microstructure models. *Additive Manufacturing* 12 (2016). Special Issue on Modeling and Simulation for Additive Manufacturing, 144–158.

[89] H. Zareie Rajani and A. Phillion. 3D multi-scale multi-physics modelling of hot cracking in welding. *Materials & Design* 144 (2018), 45–54.

[90] G. Moeini, A. Ramazani, J. Hildebrand, C. Roessler, and C. Koenke. Study of the effect of microstructural variation on the low cycle fatigue behavior of laser welded DP600 steel: Simulation and experimental validation. *Materials Science and Engineering: A* 730 (2018), 232–243.

[91] *Abaqus Analysis User's Manual*. 2018th ed. Providence, Rhode Island USA: Dassault Systèmes Simulia Corp, 2018.

[92] L. Börjesson and L. E. Lindgren. Simulation of multipass welding with simultaneous computation of material properties. *Journal of Engineering Materials and Technology, Transactions of the ASME* 123.1 (2001), 106–111.

[93] L. E. Lindgren. "Modelling for residual stresses and deformations due to welding : "knowing what isn't necessary to know"." *Mathematical Modelling of Weld Phenomena 6 :* Maney Publishing (for The Institute of Materials, Minerals and Mining), 2002, pp. 491–518.

[94] P. Dong. Residual stresses and distortions in welded structures: a perspective for engineering applications. *Science and Technology of Welding and Joining* 10.4 (2005), 389–398.

[95] L. E. Lindgren. *Computational welding mechanics: Thermomechanical and Microstructural Simulations*. Woodhead Publishin Limited, 2007.

[96] S. Edalatpour, A. Saboonchi, and S. Hassanpour. Effect of phase transformation latent heat on prediction accuracy of strip laminar cooling. *Journal of Materials Processing Technology* 211.11 (2011), 1776–1782.

[97] T. Wu, M. Coret, and A. Combescure. Numerical simulation of welding induced damage and residual stress of martensitic steel 15-5PH. *International Journal of Solids and Structures* 45.18 (2008), 4973–4989.

[98] D. Deng and H. Murakawa. Numerical simulation of temperature field and residual stress in multi-pass welds in stainless steel pipe and comparison with experimental measurements. *Computational Materials Science* 37.3 (2006), 269–277.

[99] A. Ekberg and E. Kabo. Fatigue of railway wheels and rails under rolling contact and thermal loading—an overview. *Wear* 258.7 (2005). Contact Mechanics and Wear of Rail/Wheel Systems, 1288–1300.

[100] J. P. Srivastava, P. K. Sarkar, and V. Ranjan. Effects of thermal load on wheel–rail contacts: A review. *Journal of Thermal Stresses* 39.11 (2016), 1389–1418.

[101] T. Xu, D. Zeng, L. Lu, G. Chen, and Q. Zou. Numerical investigation of the formation of white etching layer in wheel steel with high Si and Mn contents. *Engineering Failure Analysis* 122 (2021), 105286.

[102] J. Seo, S. Kwon, H. Jun, and D. Lee. Numerical stress analysis and rolling contact fatigue of White Etching Layer on rail steel. *International Journal of Fatigue* 33.2 (2011), 203–211.

[103] L. Thiercelin, L. Saint-Aimé, F. Lebon, and A. Saulot. Thermomechanical modelling of the tribological surface transformations in the railroad network (white etching layer). *Mechanics of Materials* 151 (2020), 103636.

[104] C. Jessop, J. Ahlström, C. Persson, and Z. Zhang. Damage evolution around white etching layer during uniaxial loading. *Fatigue and Fracture of Engineering Materials and Structures* May (2019), 1–8.

[105] J. Ahlström and B. Karlsson. Microstructural evaluation and interpretation of the mechanically and thermally affected zone under railway wheel flats. *Wear* 232.1 (1999), 1–14.

[106] K. Runesson, A. Skyttebol, and L.-E. Lindgren. "Nonlinear Finite Element Analysis and Applications to Welded Structures". *Comprehensive Structural Integrity*. Ed. by I. Milne, R. Ritchie, and B. Karihaloo. Oxford: Pergamon, 2003, pp. 255–320.

[107] M. T. S Okano and M. Mochizuki. Arc physics based heat source modelling for numerical simulation of weld residual stress and distortion. *Science and Technology of Welding and Joining* 16.3 (2011), 209–214.

[108] L. Wang, J. Chen, S. Zhang, and C. Wu. Numerical simulation of coupled arc-droplet-weld pool behaviors during compound magnetic field assisted gas metal arc welding. *AIP Advances* 11.6 (2021), 065221.

[109] Z. Yang, S. Sista, J. Elmer, and T. DebRoy. Three dimensional Monte Carlo simulation of grain growth during GTA welding of titanium. *Acta Materialia* 48.20 (2000), 4813–4825.

[110] L. Wang, Y. Huang, D. Yang, H. Li, Y. Peng, and K. Wang. Multi-scale simulation of grain growth during laser beam welding of nickel-based superalloy. *Journal of Materials Research and Technology* 9.6 (2020), 15034–15044.

[111] X. Yu, J. L. Caron, S. S. Babu, J. C. Lippold, D. Isheim, and D. N. Seidman. Strength Recovery in a High-Strength Steel During Multiple Weld Thermal Simulations. *Metallurgical and Materials Transactions A* 42.12 (2011), 3669–3679.

[112] G. K. Priya, M. J. Deepu, P. Venkatesh, and G. Phanikumar. Integrated Computational Materials Engineering-Based Simulation of Detrimental Precipitates in Power Plant Steel Weld. *Journal of Materials Engineering and Performance* 30.3 (2021), 1544–1024.

[113] L. E. Lindgren, H. Runnemalm, and M. O. Näsström. Simulation of multipass welding of a thick plate. *International Journal for Numerical Methods in Engineering* 44.9 (1999), 1301–1316.

[114] K. Seleš, M. Perić, and Z. Tonković. Numerical simulation of a welding process using a prescribed temperature approach. *Journal of Constructional Steel Research* 145 (2018), 49–57.

[115] D. Deng and H. Murakawa. Prediction of welding distortion and residual stress in a thin plate butt-welded joint. *Computational Materials Science* 43.2 (2008), 353–365.

[116] P. K. Taraphdar, R. Kumar, C. Pandey, and M. M. Mahapatra. Significance of Finite Element Models and Solid-State Phase Transformation on the Evaluation of Weld Induced Residual Stresses. *Metals and Materials International* 27.9 (2021), 3478–3492.

[117] J. Hu and H. Tsai. Heat and mass transfer in gas metal arc welding. Part I: The arc. *International Journal of Heat and Mass Transfer* 50.5 (2007), 833–846.

[118] T. Eagar and N. Tsai. Temperature fields produced by traveling distributed heat sources. *Welding journal* 62.12 (1983), 346–355.

[119] J. Goldak, A. Chakravarti, and M. Bibby. A New Finite Element Model for Welding Heat Sources. *Metallurgical Transactions B* 15.June (1984), 299–305.

[120] J. Goldak, M. Bibby, J. Moore, R. House, and B. Patel. Computer modeling of heat flow in welds. *Metallurgical transactions B* 17.3 (1986), 587–600.

[121] R. Spina, L. Tricarico, G. Basile, and T. Sibillano. Thermo-mechanical modeling of laser welding of AA5083 sheets. *Journal of Materials Processing Technology* 191.1 (2007). Advances in Materials and Processing Technologies, July 30th - August 3rd 2006, Las Vegas, Nevada, 215–219.

[122] R. Farias, P. Teixeira, and L. Vilarinho. An efficient computational approach for heat source optimization in numerical simulations of arc welding processes. *Journal of Constructional Steel Research* 176 (2021), 106382.

[123] S. Lorin, J. Madrid, R. Söderberg, and K. Wärmefjord. A New Heat Source Model for Keyhole Mode Laser Welding. *Journal of Computing and Information Science in Engineering* 22.1 (2021), 011004.

[124] D. Gery, H. Long, and P. Maropoulos. Effects of welding speed, energy input and heat source distribution on temperature variations in butt joint welding. *Journal*

of Materials Processing Technology 167.2 (2005). 2005 International Forum on the Advances in Materials Processing Technology, 393–401.

[125] H. Long, D. Gery, A. Carlier, and P. Maropoulos. Prediction of welding distortion in butt joint of thin plates. *Materials & Design* 30.10 (2009), 4126–4135.

[126] D. Deng, Y. Zhou, T. Bi, and X. Liu. Experimental and numerical investigations of welding distortion induced by CO2 gas arc welding in thin-plate bead-on joints. *Materials & Design (1980-2015)* 52 (2013), 720–729.

[127] H.-K. Jun, J.-W. Seo, I.-S. Jeon, S.-H. Lee, and Y.-S. Chang. Fracture and fatigue crack growth analyses on a weld-repaired railway rail. *Engineering Failure Analysis* 59 (2016), 478–492.

[128] H. K. Jun, D. W. Kim, I. S. Jeon, S. H. Lee, and Y. S. Chang. Investigation of residual stresses in a repair-welded rail head considering solid-state phase transformation. *Fatigue & Fracture of Engineering Materials & Structures* 40.7 (2017), 1059–1071.

[129] B. Q. Chen, M. Hashemzadeh, and C. Guedes Soares. Numerical and experimental studies on temperature and distortion patterns in butt-welded plates. *International Journal of Advanced Manufacturing Technology* 72.5-8 (2014), 1121–1131.

[130] M. Attarha and I. Sattari-Far. Study on welding temperature distribution in thin welded plates through experimental measurements and finite element simulation. *Journal of Materials Processing Technology* 211.4 (2011), 688–694.

[131] D. Kollár, B. Kövesdi, L. G. Vigh, and S. Horváth. Weld process model for simulating metal active gas welding. *International Journal of Advanced Manufacturing Technology* 102.5-8 (2019), 2063–2083.

[132] S. Lorin, C. Cromvik, F. Edelvik, and R. Söderberg. Welding Simulation of Non-Nominal Structures With Clamps. *Journal of Computing and Information Science in Engineering* 15.2 (2015), 021004.

[133] P. Dong and F. W. Brust. Welding Residual Stresses and Effects on Fracture in Pressure Vessel and Piping Components: A Millennium Review and Beyond. *Journal of Pressure Vessel Technology* 122.3 (2000), 329–338.

[134] C. Liu, J. Zhang, and C. Xue. Numerical investigation on residual stress distribution and evolution during multipass narrow gap welding of thick-walled stainless steel pipes. *Fusion Engineering and Design* 86.4 (2011), 288–295.

[135] L. E. Lindgren. Finite element modeling and simulation of welding part 1: Increased complexity. *Journal of Thermal Stresses* 24.2 (2001), 141–192.

[136] P. Michaleris. Residual stress distributions for multi-pass welds in pressure vessel and piping components. *ASME-Puplications-PVP* 327 (1996), 17–28.

[137] L. E. Lindgren and E. Hedblom. Modelling of addition of filler material in large deformation analysis of multipass welding. *Communications in Numerical Methods in Engineering* 17.9 (2001), 647–657.

[138] A. Lundbäck and L. E. Lindgren. Modelling of metal deposition. *Finite Elements in Analysis and Design* 47.10 (2011), 1169–1177.

[139] A. S. Oddy, J. M. J. McDill, and J. A. Goldak. Consistent Strain Fields in 3D Finite Element Analysis of Welds. *Journal of Pressure Vessel Technology* 112.3 (1990), 309–311.

[140] S. de Miranda and F. Ubertini. On the consistency of finite element models in thermoelastic analysis. *Computer Methods in Applied Mechanics and Engineering* 190.18 (2001), 2411–2427.

[141] G. Prathap and B. Naganarayana. Consistent thermal stress evaluation in finite elements. *Computers & Structures* 54.3 (1995), 415–426.

[142] L.-E. Lindgren, H.-A. Häggblad, J. McDill, and A. Oddy. Automatic remeshing for three-dimensional finite element simulation of welding. *Computer Methods in Applied Mechanics and Engineering* 147.3 (1997), 401–409.

[143] H. Runnemalm and S. Hyun. Three-dimensional welding analysis using an adaptive mesh scheme. *Computer Methods in Applied Mechanics and Engineering* 189.2 (2000), 515–523.

[144] M. Näsström, L. Wikander, L. Karlsson, L. E. Lindgren, and J. Goldak. "Combined Solid and Shell Element Modelling of Welding". *Mechanical Effects of Welding*. Ed. by L. Karlsson, L. E. Lindgren, and M. Jonsson. Berlin, Heidelberg: Springer Berlin Heidelberg, 1992, pp. 197–205.

[145] J. McDill, K. Runnemalm, and A. Oddy. An 8- to 16-node solid graded shell element for far-field applications in 3-D thermal-mechanical FEA. *Journal of Mathematical Modelling and Scientific Computing* 13.3 (2001), 177–190.

[146] D. Karalis. Increasing the efficiency of computational welding mechanics by combining solid and shell elements. *Materials Today Communications* 22 (2020), 100836.

[147] T. Kik. Computational Techniques in Numerical Simulations of Arc and Laser Welding Processes. *Materials* 13.3 (2020).

[148] S. H. Lee, S. H. Kim, Y. S. Chang, and H. K. Jun. Fatigue life assessment of railway rail subjected to welding residual and contact stresses. *Journal of Mechanical Science and Technology* 28.11 (2014), 4483–4491.

[149] C. Liu, Y. Luo, M. Yang, and Q. Fu. Three-dimensional finite element simulation of welding residual stress in RPV with two J-groove welds. English. *Welding in the World* 61.1 (2017), 151–160.

[150] X. Hu, G. Feng, Y. Wang, C. Zhang, and D. Deng. Influence of lumping passes on calculation accuracy and efficiency of welding residual stress of thick-plate butt joint in boiling water reactor. *Engineering Structures* 222 (2020), 111136.

[151] A. Malmelöv, A. Lundbäck, and L. E. Lindgren. History Reduction by Lumping for Time-Efficient Simulation of Additive Manufacturing. *Metals* 10.1 (2020).

[152] A. Kiran, J. Hodek, J. Vavřík, M. Urbánek, and J. Džugan. Numerical Simulation Development and Computational Optimization for Directed Energy Deposition Additive Manufacturing Process. *Materials* 13.11 (2020).

[153] H. Murakawa, D. Deng, N. Ma, and J. Wang. Applications of inherent strain and interface element to simulation of welding deformation in thin plate structures. *Computational Materials Science* 51.1 (2012), 43–52.

[154] J. Zhu, M. Khurshid, I. Barsoum, and Z. Barsoum. Computational weld-mechanics assessment of welding distortions in a large beam structure. *Engineering Structures* 236 (2021), 112055.

[155] Z. Barsoum and A. Lundbäck. Simplified FE welding simulation of fillet welds – 3D effects on the formation residual stresses. *Engineering Failure Analysis* 16.7 (2009), 2281–2289.

[156] Z. Barsoum and I. Barsoum. Residual stress effects on fatigue life of welded structures using LEFM. *Engineering Failure Analysis* 16.1 (2009), 449–467.

[157] S. Sarkani, V. Tritchkov, and G. Michaelov. An efficient approach for computing residual stresses in welded joints. *Finite Elements in Analysis and Design* 35.3 (2000), 247–268.

[158] H.-S. Shin and S.-H. Boo. Welding simulation using a reduced order model for efficient residual stress evaluation. *Journal of Computational Design and Engineering* 9.4 (2022), 1196–1213.

[159] R. R. Porcaro, G. L. Faria, L. B. Godefroid, G. R. Apolonio, L. C. Cândido, and E. S. Pinto. Microstructure and mechanical properties of a flash butt welded pearlitic rail. *Journal of Materials Processing Technology* 270 (2019), 20–27.

[160] A. Allie, H. Aglan, and M. Fateh. Microstructure-fracture behavior relationships of slot-welded rail steels. *Metallurgical and Materials Transactions A* 42.9 (2011), 2706–2715.

[161] D. Tawfik, P. J. Mutton, and W. K. Chiu. Experimental and numerical investigations: Alleviating tensile residual stresses in flash-butt welds by localised rapid post-weld heat treatment. *Journal of Materials Processing Technology* 196.1 (2008), 279–291.

[162] E. Kabo, A. Ekberg, and M. Maglio. Rolling contact fatigue assessment of repair rail welds. *Wear* 436-437 (2019), 203030.

[163] *Banöverbyggnad - Svetsning, bearbetning och smörjning.* Tech. rep. TRVINFRA-00016. Borlänge, Sweden: Trafikverkets infrastrukturregelverk, 2022.

[164] *Svetsning av räler och rälskomponenter. Svetsarprövning.* Tech. rep. TDOK 2014:0587. Borlänge, Sweden: Trafikverkets infrastrukturregelverk, 2018.

[165] *Svetsning av räler och rälskomponenter. Godkännande av svetsprocedurer.* Tech. rep. TDOK 2014:0586. Borlänge, Sweden: Trafikverkets infrastrukturregelverk, 2018.

[166] J. Li, W. Fan, Y. Liu, and W. Wang. Experimental and simulation research on residual stress for abrasive belt rail grinding. *The International Journal of Advanced Manufacturing Technology* 149.1 (2020), 129–142.

[167] S. Kallander. Rail Maintinance Specialist, The Swedish Transport Administration. Personal communication, regarding confidential accident reports regarding rail fractures. 2023-04-18.

[168] C. Zhang, C. Shen, X. Hua, F. Li, Y. Zhang, and Y. Zhu. Influence of wire-arc additive manufacturing path planning strategy on the residual stress status in one single buildup layer. *The International Journal of Advanced Manufacturing Technology* 111 (2020), 797–806.

[169] R. Li, G. Wang, X. Zhao, F. Dai, C. Huang, M. Zhang, X. Chen, H. Song, and H. Zhang. Effect of path strategy on residual stress and distortion in laser and cold metal transfer hybrid additive manufacturing. *Additive Manufacturing* 46 (2021), 102203.

[170] A. Skyttebol, B. Josefson, and J. Ringsberg. Fatigue crack growth in a welded rail under the influence of residual stresses. *Engineering Fracture Mechanics* 72.2 (2005). Fracture Mechanics in Railway Applications, 271–285.

[171] D. F. Cannon, K.-O. Edel, S. L. Grassie, and K. Sawley. Rail defects: an overview. *Fatigue & Fracture of Engineering Materials & Structures* 26.10 (2003), 865–886.

[172] K. Kondo, K. Yoroizaka, and Y. Sato. Cause, increase, diagnosis, countermeasures and elimination of Shinkansen shelling. *Wear* 191.1 (1996). 4th International Conference on Contact Mechanics and Wear of Rail-Wheel Systems, 199–203.

[173] H. H. Meißner K. "Detektion und Behandlung von Schienenfehlern in Gleisen und Weichen der DB Netz AG". *Internationales Symposium "Schienenfehler", Brandenburg*. Ed. by E. K-O. Brandenburg, Germany: Der Rektor der Fachhochschule Brandenburg, 2000.

[174] P. Mutton and E. Alvarez. Failure modes in aluminothermic rail welds under high axle load conditions. *Engineering Failure Analysis* 11.2 (2004). Papers presented at the International Conference on Failure Analysis ICFA, 151–166.

[175] D. Tawfik, O. Kirstein, P. J. Mutton, and W. K. Chiu. Verification of residual stresses in flash-butt-weld rails using neutron diffraction. *Physica B: Condensed Matter* 385-386 (2006), 894–896.

[176] Z. Wen, G. Xiao, X. Xiao, X. Jin, and M. Zhu. Dynamic vehicle–track interaction and plastic deformation of rail at rail welds. *Engineering Failure Analysis* 16.4 (2009), 1221–1237.

[177] W. Li, G. Xiao, Z. Wen, X. Xiao, and X. Jin. Plastic deformation of curved rail at rail weld caused by train–track dynamic interaction. *Wear* 271.1 (2011). Proceedings of the 8th International Conference on Contact Mechanics and Wear of Rail / Wheel Systems, Florence, 2009, 311–318.

[178] C. Feddersen, R. Buchheit, D. Broek, et al. *Fatigue Crack Propagation in Rail Steels*. Tech. rep. United States. Federal Railroad Administration, 1977.

[179] H. Mansouri and A. Monshi. Microstructure and residual stress variations in weld zone of flash-butt welded railroads. *Science and Technology of Welding and Joining* 9.3 (2004), 237–245.

[180] X. Y. Fang, H. N. Zhang, D.-W. Ma, Z. J. Wu, and W. Huang. Influence of welding residual stress on subsurface fatigue crack propagation of rail. *Engineering Fracture Mechanics* 271 (2022), 108642.

[181] C. Lu, J. Nieto, I. Puy, J. Melendez, and J. Martínez-Esnaola. Fatigue prediction of rail welded joints. *International Journal of Fatigue* 113 (2018), 78–87.

[182] Y. Wu, C. L. Pun, H. Su, P. Huang, D. Welsby, P. Mutton, and W. Yan. Numerical study on ratcheting performance of heavy haul rail flash-butt welds in curved tracks. *Engineering Failure Analysis* 140 (2022), 106611.

[183] B. L. Gedney and D. C. Rizos. Combining welding-induced residual stress with thermal and mechanical stress in continuous welded rail. *Results in Engineering* 16 (2022), 100777.

[184] R. Skrypnyk, M. Ekh, J. Nielsen, and B. Pålsson. Prediction of plastic deformation and wear in railway crossings – Comparing the performance of two rail steel grades. *Wear* 428-429 (2019).

[185] R. Skrypnyk, J. Nielsen, M. Ekh, and B. Pålsson. Metamodelling of wheel–rail normal contact in railway crossings with elasto-plastic material behaviour. *Engineering with Computers* (2018).

[186] C. Ansin, B. Pålsson, M. Ekh, F. Larsson, and R. Larsson. Simulation and Field Measurements of the Long-term Rail Surface Damage due to Plasticity, Wear and Surface Rolling Contact Fatigue Cracks in a Curve. *Proceedings of the 12th International Conference on Contact Mechanics and Wear of Rail/Wheel Systems* (2022), 591–601.

[187] B. L. Josefson. "Welding of rails and effects of crack initiation and propagation". *Encyclopedia of Thermal Stresses*. Ed. by R. B. Hetnarski. Rochester, USA: Springer, Dordrecht, 2014, pp. 6589–6594.

[188] B. L. Josefson and J. W. Ringsberg. Assessment of uncertainties in life prediction of fatigue crack initiation and propagation in welded rails. *International Journal of Fatigue* 31.8 (2009), 1413–1421.

[189] I. Salehi, A. Kapoor, and P. Mutton. Multi-axial fatigue analysis of aluminothermic rail welds under high axle load conditions. *International Journal of Fatigue* 33.9 (2011), 1324–1336.

[190] M. Pletz, K. A. Meyer, D. Künstner, S. Scheriau, and W. Daves. Cyclic plastic deformation of rails in rolling/sliding contact –quasistatic FE calculations using different plasticity models. *Wear* 436-437 (2019), 202992.

[191] K. A. Meyer, R. Skrypnyk, and M. Pletz. Efficient 3d finite element modeling of cyclic elasto-plastic rolling contact. *Tribology International* 161 (2021), 107053.

[192] A. Draganis, F. Larsson, and A. Ekberg. Finite element analysis of transient thermomechanical rolling contact using an efficient arbitrary Lagrangian–Eulerian description. *Computational Mechanics* 54.2 (2014), 389–405.

[193] E. K. Robin Andersson Peter T. Torstensson and F. Larsson. An efficient approach to the analysis of rail surface irregularities accounting for dynamic train–track interaction and inelastic deformations. *Vehicle System Dynamics* 53.11 (2015), 1667–1685.